

# Anomalous HCN emission from warm giant molecular clouds

Javier R. Goicoechea<sup>1</sup>, François Lique<sup>2</sup>, and Miriam G. Santa-Maria<sup>1</sup>

<sup>1</sup> Instituto de Física Fundamental (CSIC). Calle Serrano 121-123, 28006, Madrid, Spain. e-mail: javier.r.goicoechea@csic.es

<sup>2</sup> Univ. Rennes, CNRS, IPR (Institut de Physique de Rennes), UMR 6251, F-35000 Rennes, France.

Received 13 September 2021 / Accepted 30 October 2021

## ABSTRACT

Hydrogen cyanide (HCN) is considered a good tracer of the dense molecular gas that serves as fuel for star formation. However, recent large-scale surveys of giant molecular clouds (GMCs) have detected extended HCN rotational line emission far from star-forming cores. Such observations often spectroscopically resolve the HCN  $J=1-0$  (partially also the  $J=2-1$  and  $3-2$ ) hyperfine structure (HFS). A precise determination of the physical conditions of the gas requires treating the HFS line overlap effects. Here, we study the HCN HFS excitation and line emission using nonlocal radiative transfer models that include line overlaps and new HFS-resolved collisional rate coefficients for inelastic collisions of HCN with both para- $H_2$  and ortho- $H_2$  (computed via the scaled-infinite order sudden approximation up to  $T_k = 500$  K). In addition, we account for the role of electron collisions in the HFS level excitation. We find that line overlap and opacity effects frequently produce anomalous HCN  $J=1-0$  HFS line intensity ratios (i.e., inconsistent with the common assumption of the same  $T_{ex}$  for all HFS lines) as well as anomalous HFS line width ratios. Line overlap and electron collisions also enhance the excitation of the higher  $J$  rotational lines. Our models explain the anomalous HCN  $J=1-0$  HFS spectra observed in the Orion Bar and Horsehead photodissociation regions. As shown in previous studies, electron excitation becomes important for molecular gas with  $H_2$  densities below a few  $10^5$   $cm^{-3}$  and electron abundances above  $\sim 10^{-5}$ . We find that when electron collisions are dominant, the relative intensities of the HCN  $J=1-0$  HFS lines can be anomalous too. In particular, electron excitation can produce low-surface-brightness HCN emission from very extended but low-density gas in GMCs. The existence of such a widespread HCN emission component may affect the interpretation of the extragalactic relationship HCN luminosity versus star-formation rate. Alternatively, extended HCN emission may arise from dense star-forming cores and become resonantly scattered by large envelopes of lower density gas. There are two scenarios – namely, electron-assisted (weakly) collisionally excited versus scattering – that lead to different HCN  $J=1-0$  HFS intensity ratios, which can be tested on the basis of observations.

**Key words.** ISM: clouds — Molecular processes — Molecular data — Radiative transfer — Line: formation

## 1. Introduction

Massive star clusters form within dense clumps inside giant molecular clouds (GMCs; Lada & Lada 2003). Finding appropriate spectroscopic tracers of the dense molecular gas ( $n_H = n(H) + 2n(H_2) \gtrsim 10^5$   $cm^{-3}$ ) and linking their line luminosity with the star formation rate is of critical importance (Gao & Solomon 2004b; Elmegreen 2007). Rotational emission from hydrogen cyanide (HCN) has long been considered as an appropriate probe for such gas reservoirs feeding for star formation. Indeed, HCN is sufficiently abundant to be detected in nearby star-forming clumps as well as in distant galaxies. With a dipole moment ( $\mu_e$ )  $\sim 30$  times higher than that of CO (0.11 D versus 2.99 D), collisional excitation of HCN rotational levels requires higher  $H_2$  densities than those needed to excite CO.

Paradoxically, recent surveys of local GMCs, mapping star-forming clumps as well as their extended cloud environment, have revealed widespread HCN  $J=1-0$  emission (e.g., Pety et al. 2017; Kauffmann et al. 2017; Nishimura et al. 2017; Shimajiri et al. 2017; Evans et al. 2020) associated with relatively low visual extinctions ( $A_V$ ); thus, it is shown to be associated with gas that may not be so dense, at several  $10^3$   $cm^{-3}$ . Indeed, translucent clouds ( $A_V \lesssim 5$  mag) show HCN emission consistent with HCN abundances up to  $\chi(HCN) \approx 10^{-8}$  (Turner et al. 1997). Even the lowest density diffuse molecular clouds ( $A_V \lesssim 1$  mag) show HCN  $J=1-0$  absorption lines

(e.g., Liszt & Lucas 2001; Godard et al. 2010) that are compatible with the HCN abundances inferred in dense clouds.

Very polar neutral molecules have large cross sections for inelastic collisions with electrons, that roughly scale according to  $\mu_e^2$  (Faure et al. 2007). This leads to collisional rate coefficients that are at least three to four orders of magnitude greater than those induced by collisions with neutral species. Electron collisions contribute to the excitation of interstellar HCN when the electron abundance (the so-called ionization fraction,  $\chi_e = n_e/n_H$ ) is  $\geq 10^{-5}$  and the  $H_2$  density is not especially high ( $< a$  few  $10^5$   $cm^{-3}$ ; e.g., Dickinson et al. 1977; Goldsmith & Kauffmann 2017). For instance, electron collisions control the weak HCN rotational excitation in diffuse clouds (Liszt 2012).

Owing to the clumpy or fractal structure of dense molecular clouds (e.g., Stutzki & Guesten 1990; Falgarone et al. 1991), the extended component of GMCs is porous to ultraviolet (UV) radiation from nearby massive stars (e.g., Boisse 1990). The maximum ionization fraction in ordinary GMCs appears in the first  $\approx 2-3$  mag of visual extinction into the neutral cloud (e.g., Hollenbach et al. 1991). At these low values for  $A_V$ , most electrons arise from the photoionization of carbon atoms; hence,  $\chi_e \approx \chi(C^+)$ ; with  $\chi(C^+) \approx 1.4 \cdot 10^{-4}$  in Orion (Sofia et al. 2004). The rims of dense molecular clouds (their photodissociation regions or PDRs) and the spatially extended GMC environment, where  $A_V$  and  $n_H$  naturally drop, exhibit high ionization fractions. At intermediate cloud depths, from  $A_V \approx 2-3$  mag to  $\approx 4-5$  mag, depending on the gas density and UV photon

flux, the ionization fraction is controlled by the gas-phase abundance of lower ionization potential elements, sulfur in particular; thus,  $\chi_e \approx \chi(\text{S}^+)$ . Observations of sulfur radio recombination lines imply  $\chi(\text{S}^+) \approx 1.4 \cdot 10^{-5}$  in the Orion Bar PDR (Goicoechea & Cuadrado 2021). Deeper inside the cloud, in the cold cores where star-formation actually takes place, the ionization fraction decreases to  $\chi_e \approx 10^{-8}$ , and  $n_e$  is negligibly low (e.g., Guelin et al. 1982; Caselli et al. 1998; Maret & Bergin 2007; Goicoechea et al. 2009; Bron et al. 2021).

Because of the nitrogen atom, HCN rotational levels possess hyperfine structure (HFS). The coupling between the nuclear spin ( $I = 1$  for  $^{14}\text{N}$ ) and the molecular rotation splits each rotational level  $J$  into three hyperfine levels (except level  $J = 0$ ). Each hyperfine level is designated by a quantum number  $F (= I + J)$  that varies between  $|I - J|$  and  $I + J$  (Fig. A.1 shows an energy diagram). The rotational transition  $J = 1-0$  has three HFS lines:  $F = 0-1$ ,  $F = 2-1$ , and  $F = 1-1$ , which are separated by  $-7.1 \text{ km s}^{-1}$  and  $+4.9 \text{ km s}^{-1}$  from the central  $F = 2-1$  line (see Fig. 1). These separations are larger than the typical line widths ( $\sim 0.5-3 \text{ km s}^{-1}$ ) seen at GMC clump scales ( $\sim 0.2-2 \text{ pc}$ ). Hence, observations of galactic disk GMCs spectrally resolve these HFS lines (or at least their intensity peaks). As in the case of other interstellar molecules with resolved HFS structure ( $\text{N}_2\text{H}^+$ ,  $\text{CF}^+$ ,  $\text{NH}_3$ ,  $\text{C}^{17}\text{O}$ ,  $\text{OH}$ , ...), the relative  $J = 1-0$  HFS line intensity ratios can provide straightforward information on the excitation temperature ( $T_{\text{ex}}$ ) and column density (e.g., Caselli et al. 2002; Guzmán et al. 2012; Punanova et al. 2018; Zhang et al. 2020). This is particularly useful as widefield emission maps usually detect a single rotational line (often the  $J = 1-0$ ). However, as we show later, detailed excitation models are needed when radiative effects become important.

In the optically thin limit ( $\tau \rightarrow 0$ ), the relative strengths of HCN  $J = 1-0$  HFS lines are 1:5:3,  $T_{\text{ex}}$  is exactly the same for the three HFS transitions and equal to  $T_k$  if local thermodynamic equilibrium (LTE) prevails. Therefore, we would expect the integrated line intensity ratios to vary from  $R_{12} = W(F=1-1)/W(F=2-1) = 3/5 = 0.6$  and  $R_{02} = W(F=0-1)/W(F=2-1) = 1/5 = 0.2$ , to  $R_{12} = 1$  and  $R_{02} = 1$  in the optically thick limit ( $\tau \rightarrow \infty$ ). However, observations of interstellar HCN mostly show anomalous HCN ratios, that is,  $R_{12}$  and  $R_{02}$  values that are out of the  $[0.6-1]$  and  $[0.2-1]$  ranges.

Early observations of warm GMCs detected anomalous  $R_{12} < 0.6$  and  $R_{02} \geq 0.2$  ratios (Gottlieb et al. 1975; Baudry et al. 1980), whereas cores in nearby cold dark clouds such as Taurus (those forming low-mass stars only, Bergin & Tafalla 2007) show a more complicated behavior, reaching  $R_{12} > 1$  and  $R_{02} > 1$  (Walmsley et al. 1982). In dark clouds, anomalous ratios prevail over large spatial scales (Cernicharo et al. 1984). More recently, higher angular resolution observations of larger samples of low- and high-mass star-forming cores confirm the ubiquity of anomalous intensity ratios (e.g., Sohn et al. 2007; Loughnane et al. 2012; Magalhães et al. 2018). As we show later in this work, anomalous HFS ratios immediately imply that a single  $T_{\text{ex}}$  cannot describe the excitation of the three  $J = 1-0$  HFS lines<sup>1</sup>.

For higher  $J$  rotational levels, HCN HFS lines get closer and, owing to bulk gas motions as well as to thermal and turbulent line broadening, most of them overlap (colored arrows in Fig. 1). As line opacities rise, these overlaps induce photon exchanges between different HFS levels and alter their populations. This leads to anomalous HFS intensity ratios (e.g., Guilloteau & Baudry 1981; Gonzalez-Alfonso & Cernicharo 1993; Turner et al. 1997).

<sup>1</sup> This is exactly the basic assumption of automatic HFS gaussian line-fitting programs: same  $T_{\text{ex}}$  and same line width for all HFS lines.

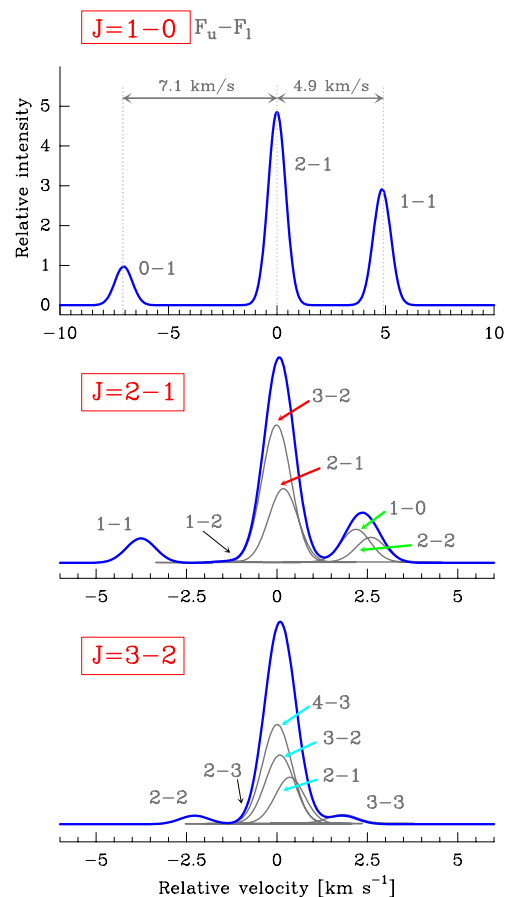


**Fig. 1.** Optically thin HCN  $J = 1-0$  ( $\sim 88.6 \text{ GHz}$ ),  $2-1$  ( $\sim 177.3 \text{ GHz}$ ) and  $3-2$  ( $\sim 265.9 \text{ GHz}$ ) spectra for a cloud with  $\Delta v \approx 1 \text{ km s}^{-1}$ . Each panel shows the velocity separation from the strongest HFS component. As line opacities increase, line overlaps in the  $J = 2-1$  and  $3-2$  HFS transitions affect the global excitation of HFS levels. Red, green, and cyan arrows show specific lines that overlap and produce most of the anomalous HFS emission discussed in the text (see also Fig. A.1).

Still, most popular large velocity gradient (LVG) radiative transfer codes do not treat HFS line overlaps. While this simplifying approach leads to reasonable results, it nonetheless *i*) misses the diagnostic power of HFS lines and *ii*) can easily lead to wrong abundances and overestimate the gas density derived from HCN, HNC, or  $\text{N}_2\text{H}^+$  observations (e.g., Daniel & Cernicharo 2008).

In this paper, we reassess the role of HFS line overlaps in the HCN emission from GMCs. We first compute new HFS-resolved rate coefficients for inelastic collisions of HCN with ortho- $\text{H}_2$  ( $I = 1$ ) and para- $\text{H}_2$  ( $I = 0$ ) at gas temperatures higher than computed before ( $T_k \leq 30 \text{ K}$  for collisions with para- $\text{H}_2$ ; Magalhães et al. 2018). We also study the HCN  $J = 1-0$  HFS anomalies in conditions relevant to the more translucent and extended GMC cloud environment that are not, thus, directly associated with dense star-forming gas. In particular, we investigate the role of HFS-resolved electron collisions and of gas velocity dispersion (line widths) in the  $R_{02}$  and  $R_{12}$  intensity ratios.

The paper is organized as follows: In Sect. 2 we briefly review the basic formalism we implemented to treat line overlap in our Monte Carlo (MTC) radiative transfer code. In Sect. 3 we present the inelastic collisional rate coefficients we use in the models. We present our model results in Sect. 4. Finally, in Sect. 5, we apply our models to the anomalous HCN  $J = 1-0$  HFS spectra observed in the Orion Bar and the Horsehead PDRs and to the low-surface-brightness HCN emission GMCs.

## 2. Background: Transfer of overlapping lines

The main difference compared to the excitation of non-overlapping lines is that a photon emitted in the HFS transition known as “ $J_F$ ”, meaning  $(J_u, F_u) \rightarrow (J_l, F_l)$ , with a frequency of  $\nu = \nu_{ul}(J_F) + \delta\nu$ , can stimulate emissions and absorptions in a different HFS transition, namely “ $J_{F'}$ ,” if their line profiles overlap<sup>2</sup>. Red, green, and cyan colored arrows in Fig. 1 show the relevant HFS overlapping lines in HCN  $J=2-1$  and  $3-2$  transitions. Photon exchanges between these lines modify the HFS level populations and the resulting mm-wave HCN spectrum compared to the case in which these exchanges are not considered. As we demonstrate here, line overlap effects result in anomalous intensity ratios for a broad range of physical conditions. In the optically thin limit ( $\tau_{ul} \rightarrow 0$ ), photon exchanges between overlapping lines tend to zero (e.g., HFS lines of the rare isotopologues  $\text{H}^{13}\text{C}^{14}\text{N}$  and  $\text{H}^{12}\text{C}^{15}\text{N}$ ). However, they become very important as line opacity increases (i.e., HFS lines of the more abundant species  $\text{HCN} = \text{H}^{12}\text{C}^{14}\text{N}$ ). For overlapping HFS lines, the total gas (line) plus dust (continuum) absorption coefficient,  $\alpha_v = \alpha_d + \alpha_g$  [ $\text{cm}^{-1}$ ], at a given velocity  $v$  of the  $J \rightarrow J-1$  rotational line profile is:

$$\alpha_v = \alpha_d + \sum_{ul=J_F} \alpha_{v,ul} = \alpha_d + \sum_{ul=J_F} \frac{hc}{4\pi} (n_l B_{lu} - n_u B_{ul}) \phi_{lu}(v), \quad (1)$$

where  $\alpha_d$  refers to the dust absorption coefficient and the sum extends to all HFS  $J_F$  lines of the  $J \rightarrow J-1$  transition. In this expression,  $n_u$  and  $n_l$  refer to the upper and lower HFS level populations in  $\text{cm}^{-3}$ ,  $B_{lu}$  and  $B_{ul}$  are the Einstein coefficients for stimulated absorption and emission respectively, and  $\phi$  is the line profile of each HFS line in the Doppler velocity space (we assume  $\phi_{lu} = \phi_{ul}$ ). In this notation, one can express the frequency of a HFS transition ( $\nu_{ul}$ ) in a group of overlapping HFS lines in terms of a relative velocity  $v_{ul,r}$  [ $\text{km s}^{-1}$ ] of the  $J \rightarrow J-1$  profile:

$$v_{ul,r} = (1 - \nu_{ul}/\nu_r) c, \quad (2)$$

where  $\nu_r$  is a reference frequency. Here, we choose that of the strongest (in intrinsic line strength) HFS component of each  $J \rightarrow J-1$  transition (see Fig. 1). The total opacity at  $v$  is then  $\tau_v = \alpha_v \Delta x$ , with  $\Delta x$  in cm.

To model line overlap effects we modified a multi-slab MTC code<sup>3</sup> that treats both spherical and plane-parallel geometries (Appendix of Goicoechea et al. 2006). With some adjustments to the original code (Bernes 1979), one can compute the number of stimulated emissions,  $s(J_{F'}, J_F)$ , that a model photon representing a number of real line photons emitted in the HFS transition,  $J_F$ , produces, as it travels through the cloud, in all overlapping transitions,  $J_{F'}$ . We successfully benchmarked our procedure and model results against the HCN HFS test problem  $\text{M}_{401}$  of Gonzalez-Alfonso & Cernicharo (1993).

In the classic Monte Carlo method for non-overlapping lines, a photon emitted in the  $J_F$  line only produces stimulated emissions in this same transition. That is to say,  $B_{ul} \bar{J}_{ul} \propto s_{ul}(J_F)$  (in

<sup>2</sup> Previous theoretical studies of HCN line overlaps include simple local escape probability and LVG models (Gottlieb et al. 1975; Guilleoteau & Baudry 1981; Zinchenko & Pirogov 1987; Turner et al. 1997), accurate nonlocal Monte Carlo and  $\Lambda$ -iteration models (Lapinov 1989; Gonzalez-Alfonso & Cernicharo 1993) and accelerated-convergence models (Daniel & Cernicharo 2008; Mullins et al. 2016).

<sup>3</sup> Since we are mostly interested in the extended GMC emission, where HCN line opacities are expected to be  $\tau_{\text{HFS}} < 100$ , we do not attempt to implement any convergence acceleration method.

Bernes formalism), where  $\bar{J}_{ul}$  is the mean intensity of the  $ul$  line at a given position of the cloud (that in turn depends, non-locally, on the physical conditions and HFS level populations in other cloud positions). With line overlap, the number of induced stimulated emissions in the  $J_{F'}$  transition at a given cloud position is:

$$s_{ul'}(J_{F'}) = \sum_{ul=J_F} s(J_{F'}, J_F), \quad (3)$$

where the sum includes all overlapping HFS lines. This is a more time consuming calculation because one has to follow each line photon and compute the number of stimulated emissions that it causes in all overlapping transitions (see also Lapinov 1989; Gonzalez-Alfonso & Cernicharo 1993). The same applies to continuum photons emitted by dust grains and the cosmic microwave background. They can now be absorbed by different HFS overlapping lines  $J_{F'}$ , depending on their line opacity ratio  $\tau_{J_{F'}} / \sum \tau_{J_F}$  at each velocity position  $v$  in the line profile.

With line overlap, the velocity-dependent source function is:

$$S_v = \frac{j_v}{\alpha_v} = \frac{j_d + j_g}{\alpha_d + \alpha_g} = \frac{j_d + \sum_{ul} j_{v,ul}}{\alpha_d + \sum_{ul} \alpha_{v,ul}}, \quad (4)$$

where  $j_d$  and  $j_g$  are the dust and HFS line emissivity coefficients:

$$j_d = \alpha_d B(T_d) ; \quad j_g = \frac{hc}{4\pi} n_u A_{ul} \phi_{ul}(v), \quad (5)$$

where  $B$  is the Planck function at a dust grain temperature,  $T_d$ , and  $A_{ul}$  is the Einstein coefficient for spontaneous emission of HFS transition,  $ul$ . In most interstellar applications, the low-lying rotational lines of HCN are not affected by dust opacity (i.e.,  $\alpha_d \rightarrow 0$ ). In this case, we can simply write the source function as:

$$S_v = \frac{1}{\alpha_g} \sum_{ul} \alpha_{v,ul} S_{ul}, \quad (6)$$

where  $S_{ul}$  is the standard velocity-independent source function,  $B(\nu_{ul}, T_{\text{ex},ul})$ , of each individual HFS line.

After a Monte Carlo simulation of the line and continuum photons, we determine the HFS level populations by solving the steady-state statistical equilibrium equations:

$$n_u \sum_{l \neq u} (R_{ul} + C_{ul}) = \sum_{l \neq u} n_l (R_{lu} + C_{lu}), \quad (7)$$

where  $C_{ul}$  and  $R_{ul}$  are the collisional and radiative pumping rates [ $\text{s}^{-1}$ ] between the HFS levels  $u$  and  $l$ . The radiative rates are:

$$R_{ul} = A_{ul} + B_{ul} \bar{J}_{ul} ; \quad R_{lu} = B_{lu} \bar{J}_{lu} ; \quad B_{ul} \bar{J}_{ul} = \sum s_{ul}, \quad (8)$$

with  $s_{ul}$  as defined in Eq. 3. For the collisional rates, we consider HFS-resolved collisions of HCN molecules with ortho- $\text{H}_2$ , para- $\text{H}_2$ , and electrons:

$$C_{ul} = k_{ul}(o\text{-H}_2) n(o\text{-H}_2) + k_{ul}(p\text{-H}_2) n(p\text{-H}_2) + k_{ul}(e^-) n(e^-), \quad (9)$$

where  $n$  [ $\text{cm}^{-3}$ ] refers to the density of each collisional partner (ortho- $\text{H}_2$ , para- $\text{H}_2$ , and  $e^-$ ) and  $k_{ul}$  [ $\text{cm}^3 \text{s}^{-1}$ ] are the temperature-dependent collisional de-excitation rate coefficients. These are obtained after detailed quantum calculations from thermal averages of the specific collision cross-sections (e.g., Roueff & Lique 2013). In addition to a correct treatment of line overlaps, these coefficients are the critical ingredients to accurately determine the excitation and line emission from any interstellar molecule. In the following section, we summarize the rate coefficients  $k_{ul}(T_k)$  that we adopted in this study.

### 3. Collisional excitation of HCN HFS levels

#### 3.1. New inelastic collisions with ortho- and para-H<sub>2</sub>

Monteiro & Stutzki (1986) calculated the first HFS-resolved HCN-He quantum collisional rate coefficients for rotational levels  $J = 0$  to 4 and  $T_k$  ranging from 10 to 30 K (with He as a surrogate for para-H<sub>2</sub>). It wasn't until much later that Ben Abdallah et al. (2012) computed the rate coefficients for the hyperfine (de-)excitation of HCN in collisions with para-H<sub>2</sub> ( $J_2 = 0$ ); we note that we use  $J_2$  here to designate the rotational level of H<sub>2</sub> and avoid confusion with the rotational level  $J$  of HCN. These authors used a potential energy surface (PES) averaged over the H<sub>2</sub> orientations. Although the work by Ben Abdallah et al. (2012) improves the accuracy of the rate coefficients compared to models using HCN-He collisional rates, these calculations consider H<sub>2</sub> as a structureless collisional partner and, as discussed by Vera et al. (2014), this approximation leads to significant inaccuracies. To overcome this issue, Magalhães et al. (2018) calculated new HCN- $p$ -H<sub>2</sub> ( $J_2 = 0$ ) HFS-resolved rate coefficients, for the lowest 25 hyperfine levels and  $T_k$  in the range 5–30 K, using the nearly exact recoupling method (Lanza & Lique 2014). These data use a full-dimension PES (Denis-Alpizar et al. 2013) and are very accurate. Unfortunately, their utility is limited to low-temperature environments (e.g., cold dark clouds and prestellar cores). This lack of HFS-resolved rates for warm gas applications motivated us to calculate the rate coefficients for HCN collisions with both para-H<sub>2</sub> ( $J_2 = 0$ ) and ortho-H<sub>2</sub> ( $J_2 = 1$ ), up to  $J = 11$  (34 HFS levels) and  $T_k \leq 500$  K. However, because of the small rotational constant of HCN and the high temperatures targeted, recoupling calculations are not feasible. Instead, we determine the HFS-resolved rate coefficients, using the scaled-infinite order sudden limit (S-IOS) approximation, from the highly accurate pure rotational rate coefficients obtained by Hernández Vera et al. (2017) in the exact close coupling method (CC). The IOS approach was first introduced by Neufeld & Green (1994) for diatom-atom collisions and later extended by Lanza & Lique (2014) to the HFS excitation of linear molecules in collisions with para-H<sub>2</sub> and ortho-H<sub>2</sub>. In practice, we scaled the CC rotational rate coefficients with the ratio of HFS and rotational IOS rate coefficients as:

$$k_{J,F,J_2 \rightarrow J',F',J_2'}^{S-IOS} = \frac{k_{J,F,J_2 \rightarrow J',F',J_2'}^{IOS} k_{J,J_2 \rightarrow J',J_2'}^{CC}}{k_{J,J_2 \rightarrow J',J_2'}^{IOS}}, \quad (10)$$

where the methodology to calculate  $k_{J,F,J_2 \rightarrow J',F',J_2'}^{IOS}$  and  $k_{J,J_2 \rightarrow J',J_2'}^{IOS}$  is described by Lanza & Lique (2014). Faure et al. (2016) previously applied this approach to the HC<sub>3</sub>N-H<sub>2</sub> system and found that the S-IOS approximation is very accurate for collisions with para-H<sub>2</sub> ( $J_2 = 0$ ), and it predicts the correct behavior at intermediate and high kinetic energies in collisions with ortho-H<sub>2</sub> ( $J_2 = 1$ ). In both cases, the agreement increases with increasing  $T_k$ .

In order to evaluate the accuracy of this method, we compared the HCN- $p$ -H<sub>2</sub> rate coefficients obtained in the S-IOS approximation at temperatures below 30 K with those of Magalhães et al. (2018). The agreement between the two data sets is better than 10-20% for the dominant rate coefficients, those corresponding to transitions with small  $\Delta J$  ( $= 1, 2, \dots$ ) or with  $\Delta J = \Delta F$ , and better than 30-50% for the others. Because the validity domain of IOS based methods increases with increasing temperature, we expect the accuracy of the new rate coefficients to be better than 10-20% for temperatures above 50 K. The dataset also includes quasi-elastic ( $\Delta J = 0$ ) collisional rate coefficients, computed from a pure IOS approach because CC elastic

**Table 1.** Collisional de-excitation rate coefficients for the HCN  $J = 1 \rightarrow 0$  ( $F = 2 \rightarrow 1$ ) transition (in powers of 10 and cm<sup>3</sup> s<sup>-1</sup>).

$T_k$	10 K	50 K	200 K
H <sub>2</sub> OPR	~0.0	0.3	2.8
$k(p\text{-H}_2)^\dagger$	2.46(-11)	2.23(-11)	2.11(-11)
$k(o\text{-H}_2)^\dagger$	1.66(-10)	1.58(-10)	1.67(-10)
$k(\text{H}_2 \text{ OPR})$	2.46E(-11)	5.34(-11)	1.29(-10)
$k(e^-)^\ddagger$	3.73(-6)	3.29(-6)	2.61(-6)

**Notes.** <sup>†</sup>This work. <sup>‡</sup>From Faure et al. (2007).

**Table 2.** Critical densities and critical ortho-H<sub>2</sub> and electron fractional abundances for the HCN  $J = 1 \rightarrow 0$  ( $F = 2 \rightarrow 1$ ) transition.

$T_k$	10 K	50 K	200 K
H <sub>2</sub> OPR	~0.0	0.3	2.8
$n_{\text{cr}}(\text{H}_2)$ [cm <sup>-3</sup> ]	9.80(+5)	4.50(+5)	1.87(+5)
$\chi_{\text{cr}}^*(o\text{-H}_2)$	0.15	0.14	0.13
$n_{\text{cr}}(e^-)$ [cm <sup>-3</sup> ]	6.45	7.31	9.22
$\chi_{\text{cr}}^*(e^-)$	6.58(-6)	1.62(-5)	4.93(-5)

rate coefficients are not available. Quasi-elastic collisions mix HFS level populations. Thus, as first discussed by Guilloteau & Baudry (1981) and Gonzalez-Alfonso & Cernicharo (1993), the absolute value of these quasi-elastic rates influences the resulting line intensities and the degree of anomalous intensity ratios. Although the low-temperature quasi-elastic collision rate coefficients calculated by Magalhães et al. (2018) are more accurate, we checked that radiative transfer models using those computed in the S-IOS approximation result in comparable line intensities and similar  $R_{12}$  and  $R_{02}$  intensity ratios (see Appendix C).

Here, we adopt HFS-resolved HCN- $p$ -H<sub>2</sub> collisional rate coefficients computed in the recoupling method for models with  $T_k \leq 30$  K (at such low temperatures the abundance of ortho-H<sub>2</sub> is low, hence collisions with ortho-H<sub>2</sub> do not play a role), and those computed in the S-IOS approximation for HCN- $o/p$ -H<sub>2</sub> collisions at  $T_k > 30$  K. We stress that until 2016, all studies of HCN HFS anomalies used scaled HCN-He rate coefficients and approximated quasi-elastic rates. However, the standard reduced-mass scaling commonly used to estimate  $k_{ul}(\text{H}_2)$  from  $k_{ul}(\text{He})$  (multiplying by 1.37) is often a crude estimation, particularly when collisions with ortho-H<sub>2</sub> are relevant (see also Walker et al. 2014).

Here we follow a more accurate treatment and explicitly account for collisions with both para-H<sub>2</sub> and ortho-H<sub>2</sub> in warm gas. We assume that the H<sub>2</sub> ortho-to-para ratio (OPR),  $n(o\text{-H}_2)/n(p\text{-H}_2)$ , is thermalized to the gas temperature, for instance: OPR( $T_k=30$  K)  $\simeq$  0.03, OPR( $T_k=60$  K)  $\simeq$  0.5, OPR( $T_k=100$  K)  $\simeq$  1.6, and OPR( $T_k=200$  K)  $\simeq$  2.8. We note, however, that particular environments such as protostellar shocks and PDRs may have H<sub>2</sub> OPRs that deviate from exact thermalization (e.g., Neufeld et al. 2006; Habart et al. 2011). As an example, Table 1 shows de-excitation rate coefficients<sup>4</sup> for the HCN  $J = 1 \rightarrow 0$  ( $F = 2 \rightarrow 1$ ) HFS transition calculated in the S-IOS approximation at different gas temperatures and OPRs.

<sup>4</sup> The full dataset of rate coefficients will be available online.

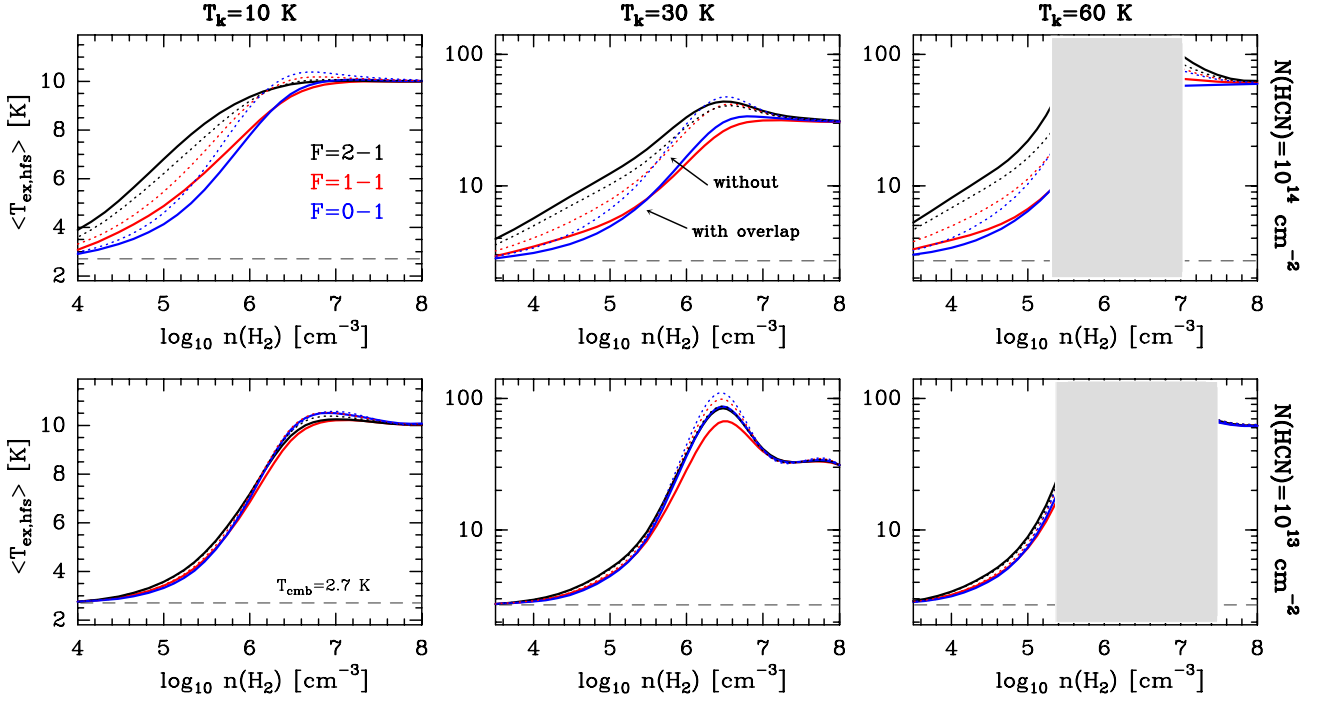


**Fig. 2.** Mean excitation temperature  $T_{\text{ex}}(F_u-F_l)$  of the three HCN  $J=1-0$  HFS lines obtained from nonlocal non-LTE models of constant density and temperature clouds with  $\Delta v_{\text{turb}} = 1 \text{ km s}^{-1}$ .  $N(\text{HCN})$  is  $10^{14} \text{ cm}^{-2}$  in the upper panels and  $10^{13} \text{ cm}^{-2}$  in the lower panels. Dotted curves show models that neglect line overlaps between different HFS lines. The gray-shaded areas are regions of the parameter space where the excitation is very suprathreshold ( $T_{\text{ex}} \gg T_k$ ) or weakly masing ( $T_{\text{ex}} < 0$  with small  $|\tau|$ ).

### 3.2. Inelastic collisions with electrons

It has long been recognized that electron collisions contribute to the rotational excitation of HCN (e.g., Dickinson et al. 1977) in environments where, first, the  $\text{H}_2$  density is not too high to thermalize a given transition;  $n(\text{H}_2)$  less than several  $10^5 \text{ cm}^{-3}$  for HCN  $J=1-0$  (e.g., Goldsmith & Kauffmann 2017) and, second, the ionization fraction is high,  $\chi_e \geq 10^{-5}$ . That is, greater than the inelastic-collision rate-coefficient ratio  $k_{ul}(\text{HCN}-\text{H}_2)/k_{ul}(\text{HCN}-e^-)$ . Here, we investigate the role of electron collisions in the HCN HFS anomalies using specific HFS-resolved  $k(\text{HCN}-e^-)$  rate coefficients calculated by Faure et al. (2007) using the IOS scaling of the  $k_{J \rightarrow J'}$  rates for  $J \leq 8$  and electron temperatures ( $T_e$ ) in the range 5–6000 K. Table 1 lists the HCN  $J=1 \rightarrow 0$  ( $F=2 \rightarrow 1$ ) de-excitation rate coefficients. Contrary to  $\text{H}_2$  collisions, electron collisions favor the  $\Delta J=1$  (dipole-like) transitions, with a strong propensity rule  $\Delta J = \Delta F$  (Faure et al. 2007). In our models (collisions with both  $\text{H}_2$  and electrons), we calculate the corresponding collisional excitation rates assuming detailed balance and  $T_k = T_e$  (thermalization).

### 3.3. Critical densities and critical fractional abundances

The density at which the collisional de-excitation rate equals the spontaneous emission rate is often referred to as the “critical density” of a given transition. For a two-level system:

$$n_{\text{cr}}(\text{H}_2 \text{ or } e^-) = \frac{A_{ul}}{k_{ul}(T_k)} [\text{cm}^{-3}]. \quad (11)$$

Table 2 shows  $n_{\text{cr}}(\text{HCN } J=1 \rightarrow 0 \text{ } F=2 \rightarrow 1)$  for different collisional partners and temperatures. In the weak collisional excitation limit ( $n \ll n_{\text{cr}}$ ) radiative effects dominate the excitation of a given transition  $ul$  and  $T_{\text{ex},ul}$  tends to  $T_{\text{cmb}} = 2.7 \text{ K}$ . In the strong collisional limit ( $n \gg n_{\text{cr}}$ ), collisions drive the excitation

toward LTE, with  $T_{\text{ex}} \approx T_k$ , and  $T_{\text{ex}}$  is the same excitation temperature for all HFS transitions. In practice, as line opacity  $\tau_{ul}$  increases, line-trapping reduces the “effective” critical density, roughly as  $n_{\text{cr,eff}} \approx n_{\text{cr}}/\tau_{ul}$  (e.g., Shirley 2015). For rotationally excited lines, the critical densities  $n_{\text{cr}}(J \rightarrow J-1)$  of the higher- $J$  HCN lines quickly increases, with  $n_{\text{cr},J=3-2} \approx 30 n_{\text{cr},J=1-0}$ .

It is also useful to define the critical electron fractional abundance,  $\chi_{\text{cr}}^*(e^-)$ , at which the electron collision rate equals the  $\text{H}_2$  rate of a given transition (e.g., Goldsmith & Kauffmann 2017). For collisions with both ortho- $\text{H}_2$  and para- $\text{H}_2$ , this implies:

$$\chi_{\text{cr}}^*(e^-) = \frac{\frac{\text{OPR}}{1+\text{OPR}} k_{ul}(o-\text{H}_2) + \frac{1}{1+\text{OPR}} k_{ul}(p-\text{H}_2)}{k_{ul}(e^-)}. \quad (12)$$

Although  $\chi_{\text{cr}}^*(e^-)$  slightly varies with temperature, electron collisions start to dominate the excitation of HCN  $J=1-0$  HFS lines at ionization fractions of about  $\geq 10^{-5}$  if  $n(\text{H}_2) < n_{\text{cr}}(\text{H}_2)$ , as shown in Table 2. Likewise, we can define the critical ortho- $\text{H}_2$  fractional abundance,  $\chi_{\text{cr}}^*(o-\text{H}_2)$  at which the  $o-\text{H}_2$  collision rate equals the  $p-\text{H}_2$  collision rate:

$$\chi_{\text{cr}}^*(o-\text{H}_2) = \frac{k_{ul}(p-\text{H}_2)}{k_{ul}(o-\text{H}_2)} = \frac{n_{\text{cr}}(o-\text{H}_2)}{n_{\text{cr}}(p-\text{H}_2)}. \quad (13)$$

Collisions with  $o-\text{H}_2$  start to dominate for  $\text{H}_2$  OPR values of  $\geq 0.15$  (Table 2), which implies gas temperatures of  $T_k > 40 \text{ K}$  if the OPR is thermalized to  $T_k$ .

## 4. Grid of HCN HFS line emission models

Here, we explore the role of line overlap and of the new collisional rate coefficients in models that cover a broad range of physical conditions relevant to the emission from GMCs. We ran a grid of single-component MTC models for HCN column densities that bracket the typical values observed in GMCs:

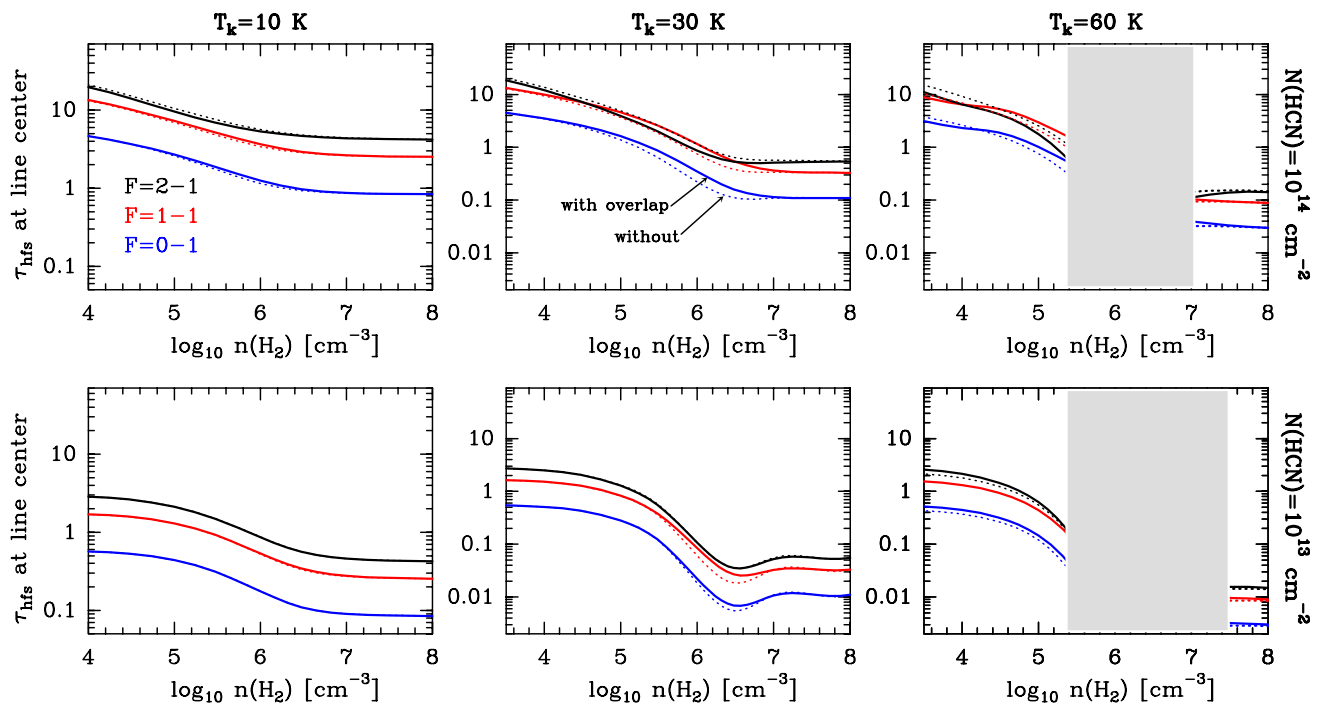


**Fig. 3.** HCN  $J = 1-0$  HFS line opacities obtained from our grid of models. Same details as in Fig. 2 but for the opacities at the line center.

$N(\text{HCN}) = 10^{13} \text{ cm}^{-2}$ , leading to optically thin or marginally thick  $J = 1-0$  HFS lines, and  $N(\text{HCN}) = 10^{14} \text{ cm}^{-2}$ , leading to optically thick lines. We cover the gas density range from  $n(\text{H}_2)$  of several  $10^3 \text{ cm}^{-3}$ , relevant to the most translucent and extended gas component of GMCs, to  $n(\text{H}_2) = 10^8 \text{ cm}^{-3}$ , which is only relevant to the inner layers of hot cores or corinos and of protostellar envelopes. There, inelastic collisions drive the excitation close to LTE. The resulting HCN line profiles include thermal, microturbulent, and opacity broadening. Velocity gradients (infall or outflows) also affect the HFS emission and can produce even more anomalous intensity ratios (for collapsing cold core models, see [Gonzalez-Alfonso & Cernicharo 1993](#); [Magalhães et al. 2018](#)). As we did not model any specific region and because we are interested in the extended GMC emission, we did not include any cloud velocity profile. Specifically, we ran spherical cloud models with uniform gas densities, temperatures ( $T_k = 10, 30, \text{ and } 60 \text{ K}$ ), and gas velocity dispersions (fixed at  $\sigma_{\text{turb}} = 0.4 \text{ km s}^{-1}$ , with  $\Delta v_{\text{turb,FWHM}} = 2.355 \sigma_{\text{turb}}$ ). However, as we use a multi-slab model (discretized in 40 shells) the excitation temperatures of the HCN HFS lines ( $T_{\text{ex,hfs}}$ ) are not necessarily uniform throughout the cloud (i.e., line excitation conditions do change) because, as opacities increase, line trapping and cloud boundary effects become important. These radiative effects, more relevant for subthermally excited ( $T_{\text{ex,hfs}} \ll T_k$ ) and optically thick lines, are not captured by standard LVG models which, in addition, neglect the radiative coupling between different cloud positions.

Since we mainly aim to study the spatially resolved emission from GMCs, we calculated the HCN column densities, line intensities, and line intensity ratios for a ray that passes through the center of the modeled spherical cloud (i.e., along a diameter). We note that more specific models of spatially unresolved emitting sources, or sources with varying physical conditions and abundances (e.g., prestellar cores), will require multiple ray tracing (i.e., involving a range of HCN column densities) and a convolution of the resulting line intensities with the telescope beam pattern at each line frequency.

#### 4.1. Changes in the HCN $J=1-0$ excitation due to line overlap

We first investigate the role of HFS line overlap neglecting electron collisions (i.e., appropriate to UV-shielded cloud environments, thus low  $\chi_e$ ). Figure 2 shows the mean excitation temperature of each HFS line ( $T_{\text{ex,hfs}}$  radially averaged over the 40 shells). Continuous curves show models that treat line overlap in all considered rotational transitions, whereas the dotted curves refer to models that do not. In the latter case, we treated the radiative excitation of each HFS line independently of the others. Figure 3 shows the line center opacity of each HFS line ( $\tau_{\text{hfs}}$ ).

The different  $T_{\text{ex,hfs}}$  values of each HFS line in Fig. 2 capture the essence of line overlap effects. At low line opacities, photon exchanges between different HFS lines are negligible and line overlap effects are irrelevant. In addition, the excitation temperature of the three  $J = 1-0$  HFS lines is nearly the same in all parameter space. This is the typical behavior for  $N(\text{HCN}) < 10^{13} \text{ cm}^{-2}$ . Since it is not easy to collisionally excite a very polar molecule such as HCN, rising  $T_{\text{ex,hfs}}$  to  $\gtrsim 4 \text{ K}$  typically requires  $n(\text{H}_2)$  above  $\approx 10^5 \text{ cm}^{-3}$  (optically thin gas and neglecting electron excitation). Beyond that, only at very high densities,  $\gtrsim 10^7 \text{ cm}^{-3}$  (strong collisional limit),  $T_{\text{ex,hfs}}$  thermalizes to the gas temperature  $T_k$ .

For optically thick HCN lines ( $\tau_{\text{hfs}} \gtrsim 1$ ) and for densities  $n(\text{H}_2) < 10^7 \text{ cm}^{-3}$ , line-trapping and line-overlap effects alter the HCN HFS level populations. Even ignoring line overlap effects, the excitation of HCN  $J = 1-0$  HFS levels is such that  $T_{\text{ex},F=2-1} > T_{\text{ex},F=1-1} > T_{\text{ex},F=0-1}$  (dotted curves in Fig. 2). [Kwan & Scoville \(1975\)](#) first proposed that these anomalous populations can be explained by the large collisional excitation from  $J = 0$  to  $J = 2$  levels (owing to the high rates  $C(J = 0 \rightarrow 2)$  in HCN- $\text{H}_2$  collisions) followed by fast radiative decay to  $J = 1$  as the  $J = 2-1$  HFS lines become optically thick. In this case, the net rate of decay from  $J = 2 \rightarrow 1$  is independent of the line strengths. For the specific range of  $\text{H}_2$  densities  $\approx 10^6 \text{ cm}^{-3}$  to  $\approx 10^7 \text{ cm}^{-3}$ , line-trapping in the  $J = 2-1$  lines reduces the popu-

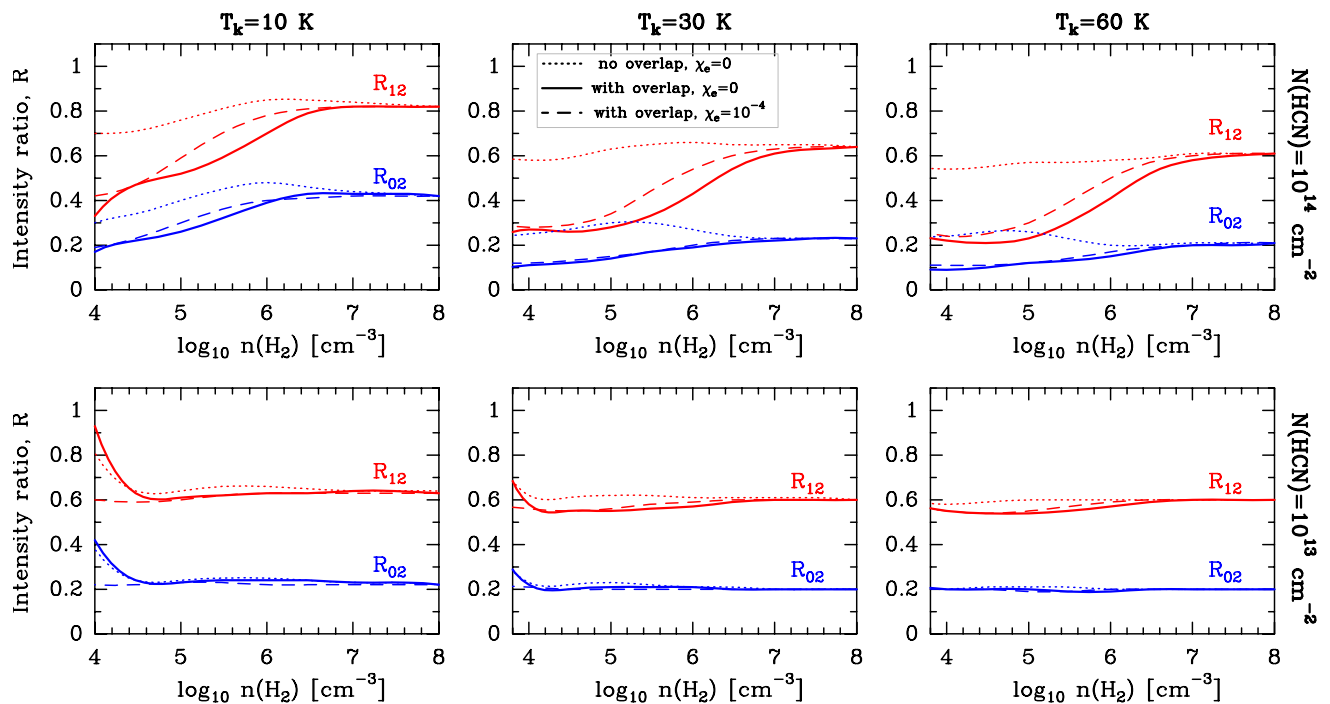


**Fig. 4.** HCN  $J = 1-0$  HFS-integrated line intensity ratios  $R_{12} = W(F=1-1)/W(F=2-1)$  and  $R_{02} = W(F=0-1)/W(F=2-1)$  obtained from our grid of models. Same details as in Fig. 2. Dashed curves are models that include line overlap and electron excitation with  $\chi_e = 10^{-4}$  (see Sect. 4.6).

lation of the  $J = 0$  level and produce suprathermal  $J = 1-0$  HFS emission ( $T_{\text{ex}} > T_k$ ).

Line overlaps in the  $J = 2-1$  and  $J = 3-2$  HFS transitions (colored arrows in Figs. 1 and A.1) lead to an increasingly efficient transfer of population from level  $J = 1, F = 1$  to level  $J = 1, F = 2$  (Guilloteau & Baudry 1981; Gonzalez-Alfonso & Cernicharo 1993). This transfer results in increased  $T_{\text{ex}, F=2-1}$  and decreased  $T_{\text{ex}, F=1-1}$  and  $T_{\text{ex}, F=0-1}$  (continuous curves in Fig. 2) compared to models that neglect line overlaps (dotted curves). For  $N(\text{HCN}) = 10^{14} \text{ cm}^{-2}$ ,  $T_k = 30 \text{ K}$ , and  $n(\text{H}_2) = 10^5 \text{ cm}^{-3}$ , the total line opacity at the center of the overlapping groups  $J = 2-1, F = 3-2$  and  $F = 2-1$  (red arrows) and  $J = 3-2, F = 4-3, F = 3-2$ , and  $F = 2-1$  (cyan arrows) is  $\tau_{J=2-1} \approx 13$  and  $\tau_{J=3-2} \approx 12$ , respectively. For  $N(\text{HCN}) = 10^{14} \text{ cm}^{-2}$  (optically thick  $J = 2-1$  lines), we predict very suprathermal emission ( $T_{\text{ex}} \gg T_k$ ) at  $T_k = 60 \text{ K}$  and  $n(\text{H}_2) \approx 10^{5.5}$  to  $\approx 10^7 \text{ cm}^{-3}$ . For  $N(\text{HCN}) = 10^{13} \text{ cm}^{-2}$  (optically thin  $J = 2-1$  lines), also at  $T_k = 60 \text{ K}$ , and similar  $n(\text{H}_2)$  range, we predict population inversions (masers,  $T_{\text{ex}} < 0$ , with small amplification factors, i.e., small  $|\tau|$ ). The shaded areas in Figs. 2 and 3 mark the parameter space of these two particular cases.

#### 4.2. Anomalous HCN $J = 1-0$ HFS line ratios $R_{12}$ and $R_{02}$

Figure 4 shows the integrated line intensity ratios  $R_{12}$  and  $R_{02}$  that result from our grid of static cloud models. Everywhere  $\tau_{\text{hfs}} \geq 1$ , models including line overlap (continuous curves) show different  $R_{12}$  and  $R_{02}$  values than models that do not (dotted curves). For HCN column densities below  $\sim 10^{13} \text{ cm}^{-2}$ , the line opacities are low, and the HCN  $J = 1-0$  HFS line ratios are always  $R_{12} \approx 0.6$  and  $R_{02} \approx 0.2$ . This is the usual case of interstellar  $\text{H}^{13}\text{CN}$  and  $\text{HC}^{15}\text{N}$  lines. As line opacities increase,  $R_{12}$  takes smaller (anomalous) values produced by the transfer of population to the  $J = 1, F = 2$  level. Hence, we expect that the HCN emission from GMCs will show anomalous  $R_{12} < 0.6$  ratios, nearly independently of  $T_k$ , for  $N(\text{HCN}) \geq 10^{13} \text{ cm}^{-2}$ . On

the other hand,  $R_{02}$  reaches values slightly above (or below) the optically thin limit of 0.2 depending on physical conditions and line widths.

Figure 5 summarizes the  $R_{12}$  and  $R_{02}$  values obtained from our grid of models. The blue curve shows the expected ratios in LTE (single  $T_{\text{ex}}$ ) as HCN column densities increase. We note that the regions of the  $R_{12}-R_{02}$  plane:  $[R_{12} > 0.6 \text{ and } R_{02} < 0.2]$ ,  $[R_{12} < R_{02}]$ , and  $[R_{12} > 1 \text{ and } R_{02} > 1]$  can not be explained by these single-component static-cloud models. They can only be interpreted by the inclusion of gas velocity gradients and absorbing envelopes of lower density gas (e.g., Gonzalez-Alfonso & Cernicharo 1993; Magalhães et al. 2018).

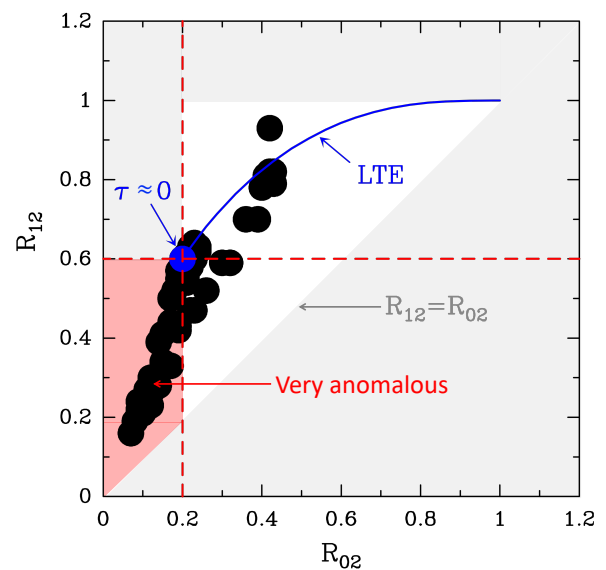


**Fig. 5.**  $R_{12}$  versus  $R_{02}$  from our grid of standard models. The blue curve shows the expected LTE ratios as HCN line opacities increase. The red shaded area shows very anomalous line intensity ratios ( $R_{12} < 0.6$  and  $R_{02} < 0.2$ ). Gray shaded areas show regions of the  $R_{12}-R_{02}$  plane that cannot be explained by single-component static cloud models.

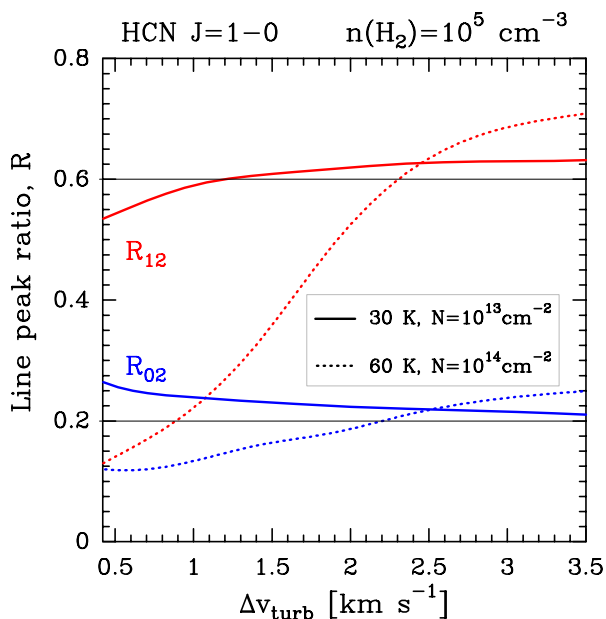


**Fig. 6.** Evolution of HCN  $J=1-0$  HFS line peak ratios  $R_{12}$  and  $R_{02}$  for increasing microturbulent velocity dispersion (line widths).

Standard LVG models such as RADEX that do not treat line overlap (e.g., Faure & Lique 2012) are not capable of explaining these anomalous ratios or the increased  $T_{\text{ex}, F=2-1}$  and reduced  $T_{\text{ex}, F=1-1}$  and  $T_{\text{ex}, F=0-1}$  values. At much higher HCN column densities ( $>10^{16} \text{ cm}^{-2}$ ) typical of the Orion hot core (e.g., Blake et al. 1987; Schilke et al. 1992), all HFS lines become very opaque and the intensity ratios tend to  $R_{12} \rightarrow 1$  and  $R_{02} \rightarrow 1$ . As a corollary, we see that for very common physical conditions and moderate columns  $N(\text{HCN})$ , the widely observed HCN  $J=1-0$  HFS lines show anomalous intensity ratios. In this case, each HFS transition has a different  $T_{\text{ex}, \text{hfs}}$  value, especially the strongest  $J=1-0$ ,  $F=2-1$  line. This is a caution against the blind application of automatic HFS fitting programs that are precisely based on the assumption of optically thin 1:5:3 intensity ratios and the same  $T_{\text{ex}}$  for all  $J=1-0$  HFS components.

#### 4.3. Role of $\Delta v_{\text{turb}}$ in the anomalous HFS line intensity ratios

Figure 6 shows the effects of line overlap for increasing microturbulent velocity dispersion (increasing line widths) in dense gas models with  $n(\text{H}_2)=10^5 \text{ cm}^{-3}$ . When intrinsic line widths increase,  $J=1-0$  HFS lines start to blend. Hence, this figure shows  $R_{12}$  and  $R_{02}$  as line peak ratios (not as integrated line intensity ratios). In general, increasing  $\Delta v_{\text{turb}}$  reduces  $\tau_{\text{hfs}}$  and makes the intensity ratios less anomalous. At low line opacities,  $R_{12}$  and  $R_{02}$  do not depend much on  $\Delta v_{\text{turb}}$  (continuous curves in Fig. 6, models with  $N(\text{HCN})=10^{13} \text{ cm}^{-2}$ ,  $T_{\text{k}}=30 \text{ K}$ , and  $\Delta v_{\text{turb}} > 1 \text{ km s}^{-1}$ ). Models with  $N(\text{HCN})=10^{14} \text{ cm}^{-2}$  and  $T_{\text{k}}=60 \text{ K}$ , however, still show anomalous ratios at  $\Delta v_{\text{turb}} \gtrsim 2 \text{ km s}^{-1}$  (dashed curves in Fig. 6) because  $\tau_{F=2-1} > 1$  and  $\tau_{F=1-1} > 1$  at all  $\Delta v_{\text{turb}}$ .

Figure 7 shows the evolution of HCN  $J=1-0$ ,  $2-1$ , and  $3-2$  line profiles as the gas velocity dispersion increases.  $J=1-0$  HFS line profiles clearly show the effects of line overlap in static and uniform clouds: brighter  $F=2-1$ , fainter  $F=1-1$  and, to a lesser extent, fainter  $F=0-1$  lines. In addition, HFS lines of higher  $J$  transitions can also show anomalous ratios. Actually, observations of low-mass star-forming cores do show anomalous HCN  $J=3-2$  HFS line intensity ratios (e.g., Loughnane et al. 2012). This rotational transition has six HFS lines, but

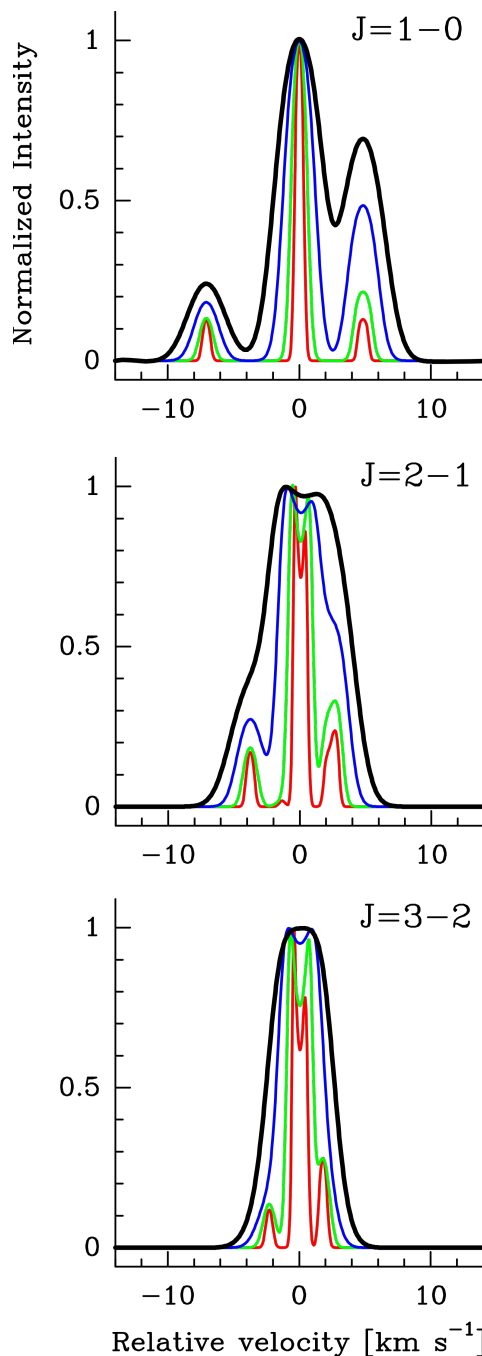


**Fig. 7.** Evolution of HCN line profiles for increasing turbulent velocity dispersion with fixed  $N(\text{HCN})=10^{14} \text{ cm}^{-2}$ ,  $T_{\text{k}}=60 \text{ K}$ , and  $n(\text{H}_2)=10^5 \text{ cm}^{-3}$ . Microturbulent line widths are  $\Delta v_{\text{turb}}=0.4 \text{ km s}^{-1}$  (red curves),  $1 \text{ km s}^{-1}$  (green),  $2 \text{ km s}^{-1}$  (blue), and  $3 \text{ km s}^{-1}$  (black).

the four central ones are blended and cannot be resolved. This gives the impression of three lines with relative intensity ratios of 1:25:1 in the optically thin limit (compare the HCN  $J=3-2$  line profiles in the lower panel of Fig. 1 with those in the right panel of Fig. 7). Higher HCN column densities and the inclusion of cloud velocity gradients will produce a greater variety of  $R_{12}$  and  $R_{02}$  values (Zinchenko & Pirogov 1987; Gonzalez-Alfonso & Cernicharo 1993; Turner et al. 1997; Mullins et al. 2016; Magalhães et al. 2018). This sensitivity to physical conditions means that HCN can be a powerful probe if their HFS lines are properly modeled.



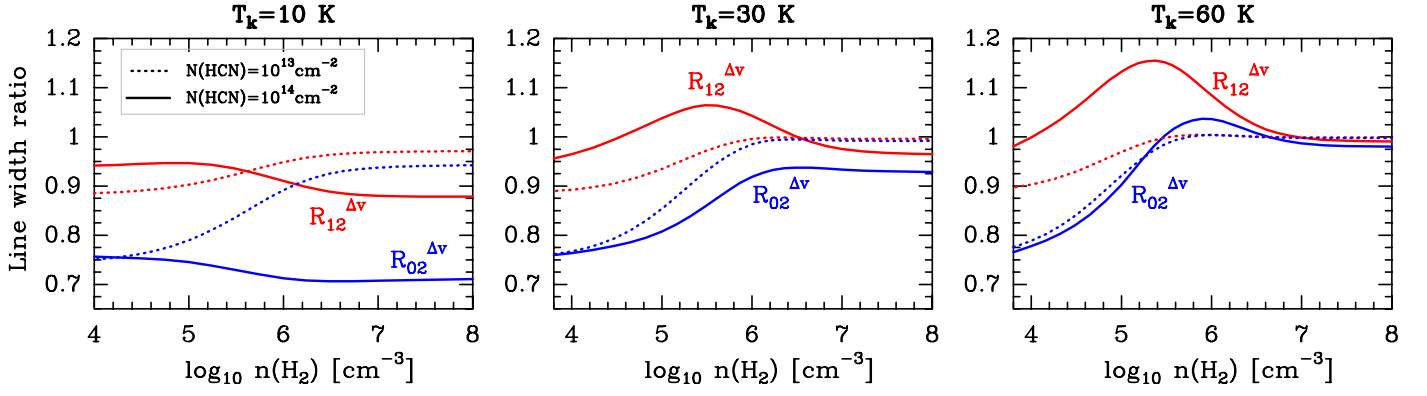


**Fig. 8.** HCN  $J=1-0$  HFS line width ratios  $R_{02}^{\Delta v} = \Delta v_{F=0-1}/\Delta v_{F=2-1}$  and  $R_{12}^{\Delta v} = \Delta v_{F=1-1}/\Delta v_{F=2-1}$  for models including line overlap.

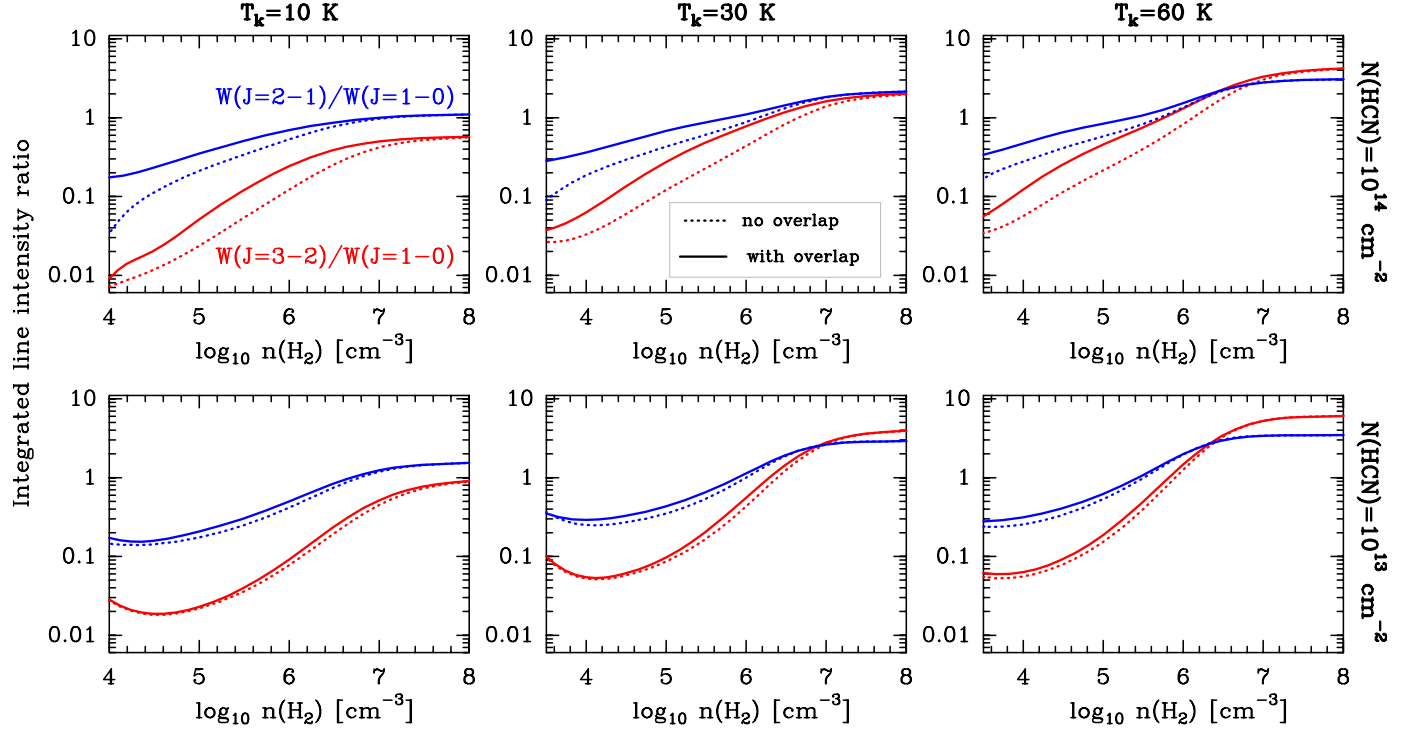


**Fig. 9.** Effect of HFS line overlap in the HCN rotational excitation. Each panel shows the integrated line intensity ratios (all HFS lines)  $W(J=2-1)/W(J=1-0)$  (blue curves) and  $W(J=3-2)/W(J=1-0)$  (red curves) for different  $N(\text{HCN})$  and  $T_k$  values, and  $W$  in units<sup>5</sup> of  $\text{K km s}^{-1}$ .

#### 4.4. Line width anomalies $R_{12}^{\Delta v}$ and $R_{02}^{\Delta v}$

In many instances not only the intensity ratios are anomalous, also the HFS line opacity ratios become anomalous (Fig. 3). The most common combination in our grid of static cloud models is  $\tau_{F=2-1} > \tau_{F=1-1} > \tau_{F=0-1}$ . Therefore, as the HFS lines become optically thick, opacity broadening will generally lead to  $\Delta v_{F=2-1} > \Delta v_{F=1-1} > \Delta v_{F=0-1}$  line widths. For two optically thick lines with the same thermal and microturbulent broadening, their line width ratio only depends on their relative opacities (Phillips et al. 1979). Hence, while in the optically thin limit  $R_{02}^{\Delta v} = \Delta v_{F=0-1}/\Delta v_{F=2-1} = 1$  and  $R_{12}^{\Delta v} = \Delta v_{F=1-1}/\Delta v_{F=2-1} = 1$ , these line width ratios also change due to anomalous line opacities produced by line overlap effects. Indeed, Loughnane et al. (2012) presented HCN  $J=1-0$  HFS detections toward G333 massive cores showing anomalous HFS line width ratios. In our grid of models, we find  $R_{02}^{\Delta v}$  ranging from  $\sim 0.71$  to  $\sim 1.03$  and  $R_{12}^{\Delta v}$  ranging from  $\sim 0.87$  to  $\sim 1.2$  (Fig. 8). This implies that the satellite line  $F=1-1$  (and less frequently the other satellite line  $F=0-1$ ) can be broader than the main HFS line  $F=2-1$ . In particular,

we predict  $R_{12}^{\Delta v} > 1$  in warm ( $T_k \geq 30$  K) and dense ( $> 10^4$   $\text{cm}^{-3}$ ) gas if the HCN column density is large,  $N(\text{HCN}) \gtrsim 10^{14}$   $\text{cm}^{-2}$ . As a complementary corollary, we conclude that the assumption of uniform HCN line widths in HFS fitting programs may not always be justified. We recommend observers to check the line width of each  $J=1-0$  HFS line individually because they may carry information about the HCN excitation conditions. When it varies, the true gas velocity dispersion should be extracted from optically thinner and not overlapped lines emitted by chemically related species.

#### 4.5. Line overlaps and the excitation of higher- $J$ HCN lines

A common misconception is that line overlap effects do not need to be treated if the cloud velocity dispersion is such that the HFS lines are sufficiently broad and, thus, the HFS structure is not spectrally resolved by observations (e.g., all HNC rotational lines and rotationally excited HCN lines). Figure 9 shows the total (all HFS lines) inte-

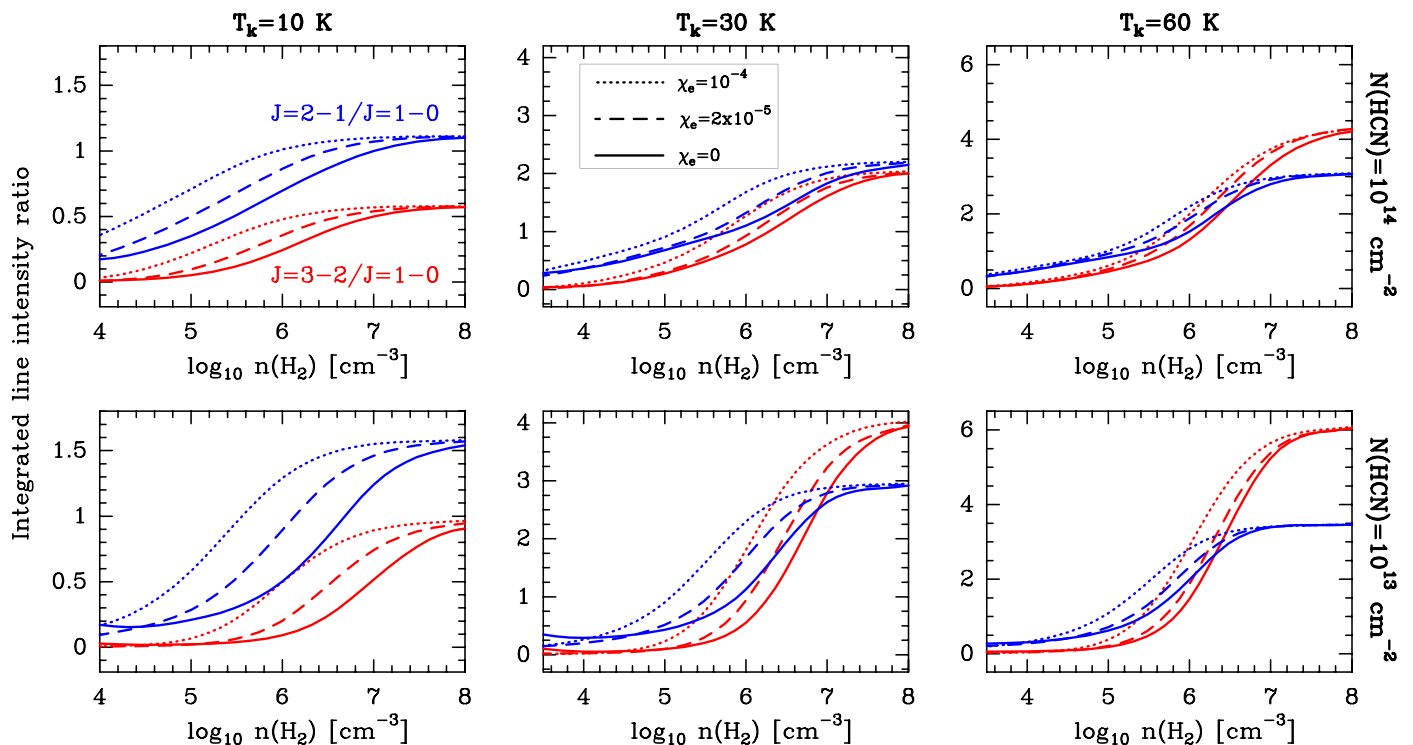


**Fig. 10.** Effects of electron excitation in the HCN rotational excitation. Each panel shows the integrated line intensity ratios  $W(J=2-1)/W(J=1-0)$  (blue curves) and  $W(J=3-2)/W(J=1-0)$  (red curves) for different  $N(\text{HCN})$  and  $T_k$  (with  $W$  in units<sup>5</sup> of  $\text{K km s}^{-1}$ ).

grated intensity ratios  $W(J=2-1)/W(J=1-0)$  (blue curves) and  $W(J=3-2)/W(J=1-0)$  (red curves) extracted from our grid of models (with  $W$  in units<sup>5</sup> of  $\text{K km s}^{-1}$ ). When line overlap effects are relevant, the excitation temperatures of the  $J=2-1$  and  $J=3-2$  HFS lines typically increase. This leads to intensity ratios  $W(J=2-1)/W(J=1-0)$  and  $W(J=3-2)/W(J=1-0)$  that are higher, by a factor of about two in our range of standard physical conditions, than the intensity ratios computed ignoring line overlaps. Hence, line overlap effects changes the  $T_{\text{ex}}$  of the higher- $J$  lines. These differences will be more pronounced at higher line opacities. We conclude that a precise analysis of the rotationally excited lines (and their intensity ratios) of abundant species such as HCN, HNC, or  $\text{N}_2\text{H}^+$  requires that their HFS line overlaps are treated (Daniel & Cernicharo 2008; Keto & Rybicki 2010). If not, parameters such as the gas density can be overestimated. A possible example is OMC-1 clump in Orion A, where observations reveal relatively extended HCN  $J=6-5$  (Goicoechea et al. 2019) and  $\text{N}_2\text{H}^+$   $J=7-6$  line emission (Hacar et al. 2020).

#### 4.6. Role of electron excitation

In Sects. 3.2 and 3.3, we anticipate that electron collisions play a role in HCN excitation when the gas ionization fraction is above the critical value of  $\chi_{\text{cr}}^*(e^-) > 10^{-5}$  (see also Dickinson et al. 1977; Liszt 2012; Goldsmith & Kauffmann 2017). Such high electron abundances are typical of the illuminated rims of GMCs (their PDRs, Goicoechea et al. 2009; Cuadrado et al. 2019) and of more extreme GMCs in galaxy nuclei, typically irradiated by enhanced doses of cosmic- and X-rays (Maloney et al. 1996; Meijerink & Spaans 2005). In addition, lower density and

<sup>5</sup> To obtain the integrated line surface brightness ratios  $I(J=2-1)/I(J=1-0)$  and  $I(J=3-1)/I(J=1-0)$  with  $I$  in units of  $\text{erg s}^{-1} \text{cm}^{-2} \text{sr}^{-1}$ , one has to multiply the ratios  $W(J=2-1)/W(J=1-0)$  and  $W(J=3-2)/W(J=1-0)$  by  $(v_{2-1}/v_{1-0})^3 \approx 8$  and  $(v_{3-2}/v_{1-0})^3 \approx 27$ .

lower UV-illumination translucent clouds also have high electron abundances (Black & van Dishoeck 1991; Hollenbach et al. 1991). In this section, we investigate the role of HFS-resolved HCN- $e^-$  collisions in this kind of environments.

Figure 4 shows the evolution of the intensity ratios  $R_{12}$  and  $R_{02}$  in line overlap models with  $\chi_e = 10^{-4}$  (dashed curves). These curves show about the maximum expected variation of  $R_{12}$  and  $R_{02}$ . In other words, lower  $\chi_e$  abundances will result in less differences (ratios similar to the case without electron collisions). In the optically thin limit, the intensity ratios do not change much, and are  $R_{12} \approx 0.6$  and  $R_{02} \approx 0.2$ . As line opacity and overlap effects become important, electron collisions lead to intensity ratios  $R_{12}$  that can be up to  $\sim 25\%$  larger (in models with  $N(\text{HCN}) = 10^{14} \text{ cm}^{-2}$ ; dashed curves) than when electron excitation does not play a role. However, the intensity ratio  $R_{02}$  in these models is nearly independent of  $\chi_e$ . Models with  $N(\text{HCN}) = 10^{13} \text{ cm}^{-2}$  and low densities,  $n(\text{H}_2) \lesssim 10^4 \text{ cm}^{-3}$ , result in marginally thick  $J=1-0$  HFS lines and intensity ratios  $R_{12} > 0.6$  and  $R_{02} > 0.2$ . Electron excitation reduces their line opacities and, thus, the intensity ratios  $R_{12}$  and  $R_{02}$  are lower (closer to 0.6 and 0.2, respectively) than when electrons are not included (see also Sect. 5.2).

We recall that excitation of polar molecules by electron collisions has a strong dipole character (i.e., dominated by  $|\Delta J|=1$  collisions) and therefore obeys different propensity rules than HCN collisions with  $\text{H}_2$ ; for which  $|\Delta J|=2$  collisions are relevant. This explains the less anomalous  $R_{12}$  values when electron collisions dominate.

As the gas density decreases below  $n_{\text{cr}}(\text{H}_2)$ , electron collisions compete with  $\text{H}_2$  collisions (at the lowest densities, electron collisions dominate). The major effect of electron collisions is to produce more intense HCN  $J=1-0$  emission when  $n(\text{H}_2) < n_{\text{cr}}(\text{H}_2; J=1-0)$  (Goldsmith & Kauffmann 2017). The intensity enhancement goes from factors of about two if  $\chi_e = 2 \cdot 10^{-5}$ , to factors of about ten if  $\chi_e = 10^{-4}$  (see

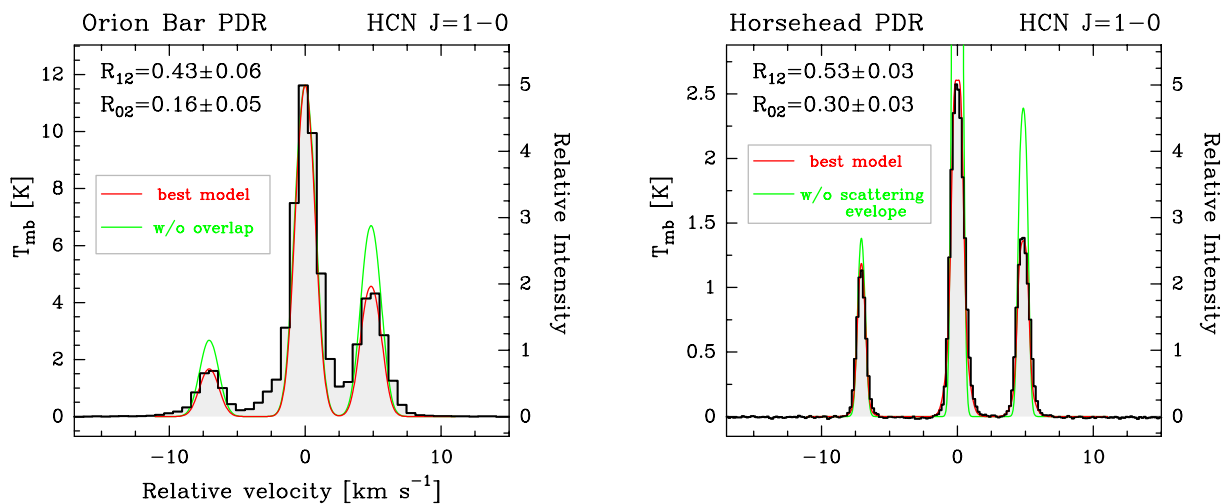


**Fig. 11.** IRAM 30 m observations and models of the HCN  $J = 1-0$  HFS lines toward the Orion Bar and the Horsehead PDRs. The intensity scale in the right axes is normalized to make clear that the observed line emission differs from the optically thin LTE line ratios 1:5:3 in both sources.

Fig. B.1). Figure 10 shows that for the same  $H_2$  density, electron collisions increase the population of the excited rotational levels, which enhances the  $W(J=2-1)/W(J=1-0)$  and  $W(J=3-2)/W(J=1-0)$  intensity ratios. The maximum effect is seen around  $n(H_2) \approx n_{cr}(H_2; J=1-0)$ , whereby  $H_2$  gas densities are not too high to thermalize the intensity ratios independently of  $\chi_e$ , but not too low so that the collisional rate is sufficiently high to appreciably populate the excited levels  $J=2$  and  $J=3$ . This means that detecting extended HCN  $J=2-1$  emission may not always imply the presence of very dense gas,  $n_{cr}(H_2; J=2-1) \approx$  a few  $10^6 \text{ cm}^{-3}$ , but lower density gas with high ionization fractions. Hence, a precise measurement of  $H_2$  densities and  $\chi(\text{HCN})$  abundances would greatly benefit from an estimation of the electron abundance of the gas where HCN emits (e.g., Bron et al. 2021).

## 5. Applications to the HCN emission from GMCs

We conclude our study by applying our models and new collisional rates to specific warm gas environments in GMCs.

### 5.1. Anomalous HCN emission from dense PDRs

In this section, we model the HCN  $J = 1-0$  HFS spectra of two prototypical dense PDRs in Orion A and B clouds: the edges of the Orion Bar and Horsehead nebula, both observed in spectral line surveys obtained with the IRAM 30 m telescope; see Cuadrado et al. (2015) and Pety et al. (2012), respectively.

The Orion Bar (strongly UV-irradiated<sup>6</sup> PDR with  $G_0 \gtrsim 10^4$ ): observed  $J = 1-0$  HFS line intensity ratios are both anomalous:  $R_{12} = 0.43 \pm 0.06$  and  $R_{02} = 0.16 \pm 0.05$ . These ratios can be explained by line overlap effects. We obtain a satisfactory fit for the following physical conditions:  $n_H \approx 2 \cdot 10^5 \text{ cm}^{-3}$ ,  $T_k \approx 100 \text{ K}$ ,  $\sigma_{\text{turb}} \approx 0.7 \text{ km s}^{-1}$ ,  $\chi_e \approx 10^{-4}$ , and  $N(\text{HCN}) \approx 10^{14} \text{ cm}^{-2}$  (beam averaged). In this single-component model assuming extended emission (red curve in the left panel of Fig. 11), the rotationally excited lines have higher opacities ( $\tau_{J=3-2} \approx 7$  at the overlapping HFS lines  $F = 4-3$ ,  $3-2$ , and  $2-1$ , and  $\tau_{J=2-1} \approx 4$  at  $F = 3-2$  and  $2-1$  lines) than the  $J = 1-0$  HFS lines ( $\tau_{J=1-0} \approx 1$ ). The excitation of these lines is subthermal,

<sup>6</sup>  $G_0$  is the flux of far-UV photons ( $E < 13.6 \text{ eV}$ ) in units of the Habing field. That is,  $G_0 = 1$  is equal to  $1.6 \cdot 10^{-3} \text{ erg cm}^{-2} \text{ s}^{-1}$ .

with  $T_{\text{ex, hfs}} \approx 10-20 \text{ K} \leq T_k = 100 \text{ K}$ . The green curve in the left panel of Fig. 11 shows a model with the same input parameters but neglecting line overlap. This model produces different line intensity ratios  $R_{12}$  and  $R_{02}$ .

The Horsehead (mildly illuminated PDR with  $G_0 \approx 100$ ): observed intensity ratios are anomalous,  $R_{12} = 0.53 \pm 0.03$  and  $R_{02} = 0.30 \pm 0.03$ . We checked that given the warm gas temperatures and moderate densities previously inferred in this PDR:  $T_k \approx 60-100 \text{ K}$  and  $n_H \approx 2 \cdot 10^4-10^5 \text{ cm}^{-3}$  (e.g., Guzmán et al. 2011; Pabst et al. 2017), a single-component cloud model can not explain these ratios. In addition, the intensity of the  $F = 0-1$  line relative to the other HFS lines, is too strong and its line width ( $\Delta v_{F=0-1} = 0.8 \pm 0.1 \text{ km s}^{-1}$ ) is narrower than those of the  $F = 2-1$  and  $F = 1-1$  lines ( $\Delta v_{F=2-1} \approx \Delta v_{F=1-1} = 1.1 \pm 0.1 \text{ km s}^{-1}$ ). These HCN line widths exceed those of the  $H^{13}\text{CN } J = 1-0$  HFS lines (not shown;  $\Delta v_{H^{13}\text{CN}} = 0.70 \pm 0.02 \text{ km s}^{-1}$ ). Hence, the  $F = 0-1/F = 2-1$  line width ratio is anomalous too, with  $R_{02}^{\Delta v} = 0.7 \pm 0.1$  and  $R_{12}^{\Delta v} = 1.0 \pm 0.1$ . These signatures suggest optically thick HCN  $J = 1-0$  lines and self-absorption of the  $F = 2-1$  and  $F = 1-1$  lines. Thus, this is a more complicated radiative transfer problem. A very likely scenario is that the edge of the Horsehead has a very steep density gradient, from diffuse to dense gas, and/or that line photons arising from the dense PDR are self-absorbed and scattered by a low density envelope.

We reproduce the anomalous HCN  $J = 1-0$  HFS spectrum with a two-component model: a moderately dense PDR with  $N(\text{HCN}) \approx 3 \cdot 10^{13} \text{ cm}^{-2}$ ,  $n_H \approx 3 \cdot 10^4 \text{ cm}^{-3}$ ,  $T_k \approx 60 \text{ K}$ ,  $\sigma_{\text{turb}} \approx 0.2 \text{ km s}^{-1}$ , and  $\chi_e \approx 10^{-4}$ , surrounded by a lower excitation envelope with:  $N(\text{HCN}) \approx 1.5 \cdot 10^{13} \text{ cm}^{-2}$ ,  $n_H \approx 4 \cdot 10^3 \text{ cm}^{-3}$ ,  $T_k \approx 30 \text{ K}$ , and  $\chi_e \lesssim 10^{-5}$  (typical of the UV-illuminated extended gas in Orion B; e.g., Pety et al. 2017). The main effect of the envelope is to absorb a fraction of the optically thick  $F = 2-1$  and  $F = 1-1$  line photons emitted from the PDR and to scatter them over large spatial scales. We note that several studies have previously argued that resonant scattering by low density envelopes or foreground clouds could explain the spatial distribution of the subthermally excited and optically thick emission from abundant high dipole moment molecules such as  $\text{HCO}^+$ , HCN, or CS, as well as their anomalous line intensities (sometimes comparable to those of their isotopologues; Langer et al. 1978; Walmsley et al. 1982; Cernicharo et al. 1984; Gonzalez-Alfonso & Cernicharo 1993; Zinchenko et al. 1993).

In our model of the Horsehead, the total line opacities are  $\tau_{F=0-1} \approx 1$ ,  $\tau_{F=2-1} \approx 5$ , and  $\tau_{F=2-1} \approx 4$ . Since the observed HFS lines do not show self-absorption dips, the gas velocity dispersion in the absorbing envelope needs to be larger ( $\sigma_{\text{turb}} \approx 0.5 \text{ km s}^{-1}$ ) than in the denser PDR. The red curve in the right panel of Fig. 11 shows the resulting line profiles. In this model the excitation temperatures of the  $J=1-0$  HFS lines are  $T_{\text{ex,hfs}} \approx 7-10 \text{ K}$  in the PDR, and  $T_{\text{ex,hfs}} \approx 3-4 \text{ K}$  in the scattering envelope. The fact that  $T_{\text{ex,hfs}}$  in the low density envelope (very weak collisional excitation) is higher than 3 K is a pure scattering effect: absorption and re-emission of line photons coming from the denser component (for cold dark cloud models, see Gonzalez-Alfonso & Cernicharo 1993). The green curve shows results of a model with the same input parameters for the dense PDR, but no scattering envelope, which results in very different intensity and line width ratios.

We finally note that the gas densities we infer in these PDRs could be slightly lower if the HCN emission arises from lower ionization fraction gas. In forthcoming papers, we will discuss more realistic models (e.g., with gradients) and analyze multiple- $J$  HCN observations of Orion B (Santa-Maria et al. in prep.) and of the Orion Bar PDR (Goicoechea et al. in prep.).

## 5.2. HCN emission from the extended environment of GMCs and whether it contributes to the extragalactic star-formation rate relation

The physical conditions in small translucent clouds:  $n(\text{H}_2)$  up to several  $10^3 \text{ cm}^{-3}$ ,  $T_{\text{k}} \approx 15-60 \text{ K}$ , and  $\chi_{\text{e}} \gtrsim 10^{-5}$  (e.g., van Dishoeck & Black 1989; Snow & McCall 2006) resemble those found in the extended environment of GMCs. These regions are very important when we consider the integrated emission from spatially unresolved GMCs in distant star-forming galaxies. Although HCN line intensities at any specific position of the extended cloud environment would be much fainter than at the dense star-forming cores ( $n(\text{H}_2) \gtrsim 10^5 \text{ cm}^{-3}$ ) – where  $\chi(\text{e}^-)$  is usually not high enough to collisionally excite HCN lines (e.g., Salas et al. 2021) – the much larger area of the extended cloud emission, the cloud envelope, means that emission lines integrated over the entire GMC can be dominated by the lower-density extended cloud and not by the dense cores (e.g., Evans et al. 2020; Santa-Maria et al. 2021). This widespread (tens of pc) and more translucent GMC environment is typically illuminated by modest stellar UV fields,  $G_0 \approx 2-100$  (e.g., Pineda et al. 2013; Abdullah & Tielens 2020) that are less extreme than the incident UV field in the dense star-forming clumps ( $\sim 1 \text{ pc}$  scales) close to young massive stars (up to  $G_0 \approx 10^5$ ; e.g., Goicoechea et al. 2019; Pabst et al. 2021).

Figure 12 shows model results appropriate to this GMC environment:  $n(\text{H}_2) = 5 \cdot 10^3 \text{ cm}^{-3}$ ,  $\Delta v_{\text{turb}} = 1 \text{ km s}^{-1}$ ,  $T_{\text{k}} = 30$  and 60 K, and  $N(\text{HCN}) = 10^{13} \text{ cm}^{-2}$  (the typical HCN column density observed in translucent clouds; Turner et al. 1997; Godard et al. 2010). Neglecting electron collisions results in very subthermal HCN emission:  $T_{\text{ex,hfs}} \lesssim 3 \text{ K}$  (see upper panel of Fig. 12), with emission levels  $I(J=1-0)$  of  $\sim 0.2 \text{ K km s}^{-1}$  and  $\sim 0.6 \text{ K km s}^{-1}$  for  $T_{\text{k}} = 30 \text{ K}$  and 60 K, respectively (lower panel of Fig. 12). For this choice of physical conditions, the opacity of the main  $J=1-0$ ,  $F=2-1$  HFS line is  $\tau_{F=2-1} \approx 2$ . That is, line overlap effects start to matter.

As the electron abundance increases, so does the excitation of the  $J \geq 1$  levels. For  $\chi_{\text{e}} \approx 10^{-5}$ , the excitation temperature of the  $J=1-0$  HFS lines starts to rise despite the  $\text{H}_2$  density being considerably lower than  $n_{\text{cr}}(\text{H}_2; J=1-0)$ . This particular  $\chi_{\text{e}}$  value leads to a  $I(J=1-0)$  enhancement by a factor of

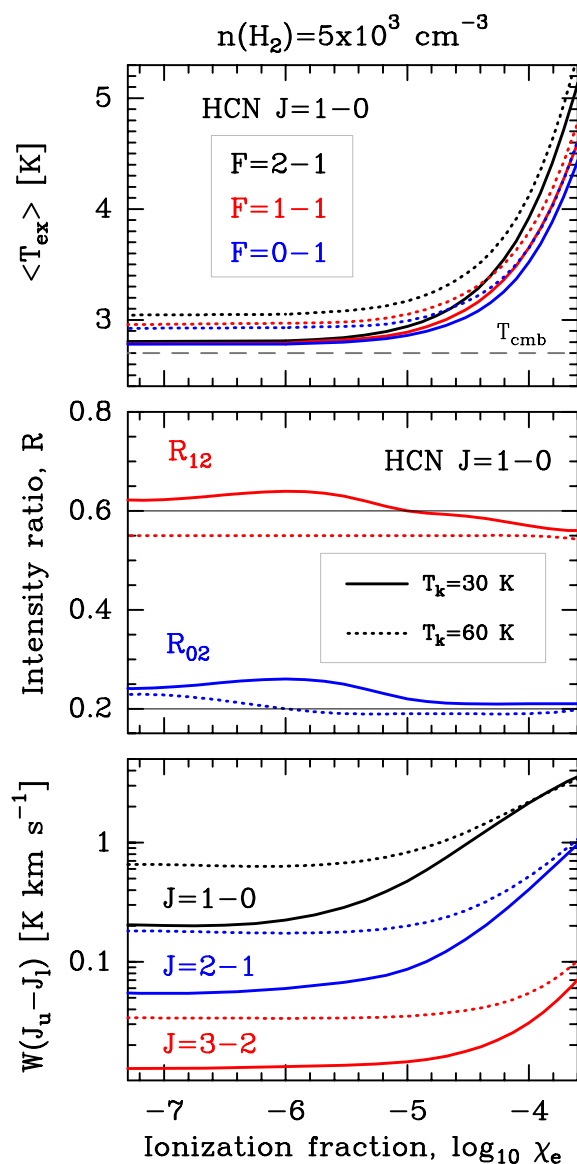


**Fig. 12.** Models of the extended and more translucent environment of GMCs as a function of the ionization fraction. For  $N(\text{HCN}) = 10^{13} \text{ cm}^{-2}$ , and  $n(\text{H}_2) = 5 \cdot 10^3 \text{ cm}^{-3}$  we show: mean  $T_{\text{ex}}(J=1-0, F_u-F_l)$  in the upper panel; line intensity ratios  $R_{02}$  and  $R_{12}$  in the middle panel; and total integrated line intensities  $\text{HCN } J=1-0, 2-1, 3-2$  in the lower panel. Continuous and dotted curves show model results for  $T_{\text{k}} = 30 \text{ K}$  and 60 K, respectively.

two. For  $\chi_{\text{e}} \approx 10^{-4}$ , excitation temperatures rise to  $T_{\text{ex,hfs}} \approx 4 \text{ K}$  and the line emission level increases up to a factor of ten,  $I(J=1-0) \approx 2 \text{ K km s}^{-1}$ , compared to models that do not include electron excitation. Because levels  $J=2$  and 3 are now more populated, the opacity of the main  $J=1-0$ ,  $F=2-1$  HFS line decreases, but it is still  $\tau_{F=2-1} \approx 1$ . We predict that in this lower density and more translucent GMC environment,  $R_{12}$  will be anomalous,  $R_{12} \lesssim 0.6$ , and the  $R_{02}$  intensity ratio could be slightly above or below 0.2, again depending on the given physical conditions and  $\Delta v$  (middle panel of Fig. 12). Despite the low  $\text{H}_2$  density, the HCN  $J=2-1$  line could be detectable, with  $I(J=2-1) \geq 0.1 \text{ K km s}^{-1}$  (Fig. B.1). Therefore, electron collisions are very important at low  $\text{H}_2$  densities, provided that HCN exists in gas with  $\chi_{\text{e}} > 10^{-5}$ , and they may contribute to the extended HCN emission in GMCs (see also Goldsmith & Kauffmann 2017).

By adopting as our references  $\chi_e = 2 \cdot 10^{-5}$  and  $T_k = 30$  K, we predict HCN line emission levels of  $I(J=1-0) \approx 0.7$  K km s $^{-1}$ . For a spherical cloud of 10 pc (or 100 pc) diameter and uniform emission, these numbers imply a integrated HCN  $J=1-0$  line luminosity (in units of K km s $^{-1}$  pc $^2$ ; Gao & Solomon 2004a) of  $L_{\text{HCN}} \approx 55$  K km s $^{-1}$  pc $^2$  (or  $\approx 5500$  K km s $^{-1}$  pc $^2$ ) considering only this extended and translucent HCN emission.

HCN  $J=1-0$  observations of a large sample of star-forming galaxies (from normal spirals to more extreme ultraluminous infrared galaxies) find the following tight relationship:

$$\dot{M}_{\text{SFR}} \approx 1.8 \cdot 10^{-7} (L_{\text{HCN}} / \text{K km s}^{-1} \text{ pc}^2) [M_{\odot} \text{ yr}^{-1}], \quad (14)$$

where  $\dot{M}_{\text{SFR}}$  is the star-formation rate (SFR) and  $L_{\text{HCN}}$  is (assumed to be) emitted by the dense molecular gas reservoir (Gao & Solomon 2004b). Inserting our  $L_{\text{HCN}}$  value in Eq. 14, we obtain  $\dot{M}_{\text{SFR}} \approx 10^{-5} M_{\odot} \text{ yr}^{-1}$  for a 10 pc cloud ( $\approx 10^{-3} M_{\odot} \text{ yr}^{-1}$  for a 100 pc cloud). We recall that these SFRs simply assume that  $L_{\text{HCN}}$  mostly arises from our toy model low-surface-brightness GMC environment. Still, the resulting  $\dot{M}_{\text{SFR}}$  rates are of the order of those inferred, from other observational tracers, toward galactic GMCs (e.g., Lada et al. 2010).

This similitude would imply that for some galaxies, the extragalactic  $\dot{M}_{\text{SFR}}-L_{\text{HCN}}$  correlation is not always dominated by emission from dense molecular gas,  $n_{\text{H}} \gtrsim 10^5$  cm $^{-3}$ . This can be the case of normal spiral galaxies in which  $L_{\text{HCN}}$  linearly correlates with  $L_{\text{CO}}$  (which is certainly dominated by extended low-density molecular gas) and also with  $L_{\text{FIR}}$ , a proxy of the SFR (Gao & Solomon 2004b). Normal galaxies have low luminosity ratios  $L_{\text{HCN}}/L_{\text{CO}} \approx 0.02-0.06$  that are interpreted as low fractions of dense molecular gas. These  $L_{\text{HCN}}/L_{\text{CO}}$  values resemble the observed ratios in modest (low SFR) GMCs such as Orion B when square-degree areas of the sky are averaged ( $L_{\text{HCN}}/L_{\text{CO}} \approx 0.025$  in  $\sim 40$  pc $^2$ ; Pety et al. 2017). Indeed, disk GMCs such as Orion A and B show more spatially extended emission in HCN than in other tracers, such as  $\text{N}_2\text{H}^+$ , of cold and dense gas (e.g., Pety et al. 2017; Kauffmann et al. 2017; Melnick et al. 2020).

Luminous and ultraluminous infrared galaxies, however, show an excess of HCN emission compared to CO ( $L_{\text{HCN}}/L_{\text{CO}} > 0.06$ ), and only  $L_{\text{HCN}}$ , not  $L_{\text{CO}}$ , is closely correlated with  $L_{\text{FIR}}$  (Gao & Solomon 2004b). Hence, the HCN emission from these more extreme (very high SFR) galaxies very likely traces a higher fraction of dense star-forming gas. According to our models, a significant fraction of the HCN luminosity at GMC scales may arise from the lower density extended component (the envelopes) of these clouds, at least in normal spirals. Since  $L_{\text{HCN}}$  and  $L_{\text{FIR}}$  (SFR) tightly correlate over three orders of magnitude in galaxies, this scenario would imply that the mass of the extended component scales with the mass of the dense star-forming cores. Careful analysis of on-going wide field molecular emission surveys of galactic GMCs (covering increasingly larger areas) are clearly needed to settle down this issue.

Interestingly, the HCN  $J=1-0$  HFS intensity ratios  $R_{12}$  and  $R_{02}$  observed in local GMCs can be used to quantify the amount of extended HCN  $J=1-0$  emission that arises from electron-assisted (weakly) collisionally excited low-density gas, versus emission from high density cores resonantly scattered over larger spatial scales by the low density cloud. In the latter case, the observed HCN luminosities will still reflect the fraction of dense molecular gas. Figure 13 shows a model example of these two scenarios. The lower panel shows the predicted intensity ratios  $R_{12}$  and  $R_{02}$  versus impact parameter (i.e., after ray tracing the spherical cloud) for a model of a dense core, with  $n(\text{H}_2) = 10^5$  cm $^{-3}$  and  $T_k = 30$  K, surrounded by a lower density envelope, with  $n(\text{H}_2) = 5 \cdot 10^3$  cm $^{-3}$ , four times

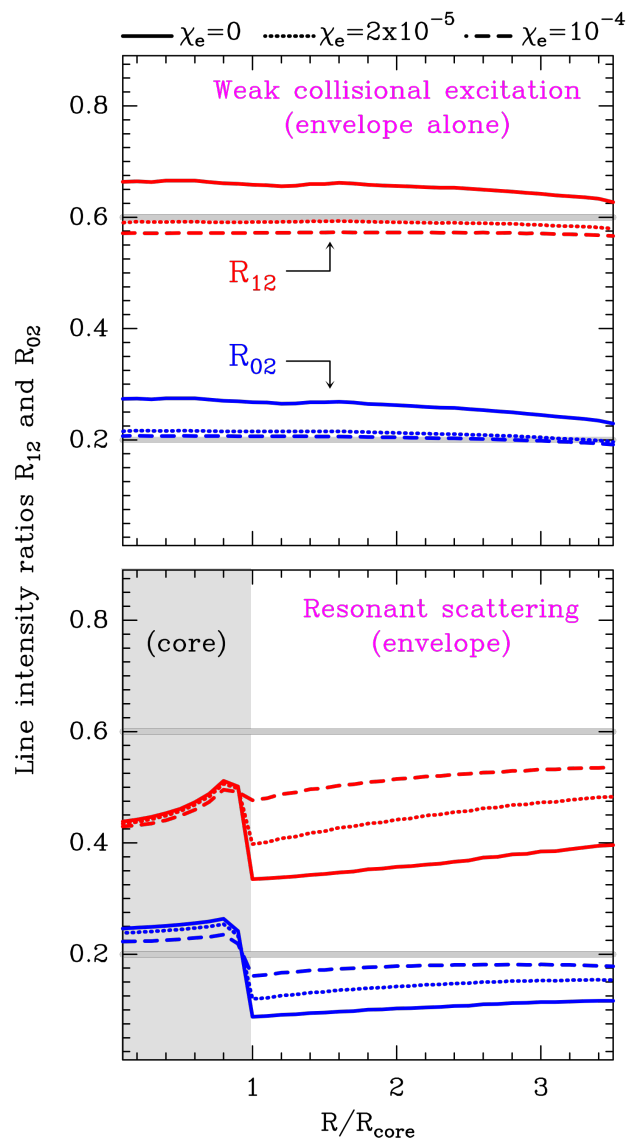


**Fig. 13.** HCN  $J=1-0$  HFS intensity ratios  $R_{12}$  (red curves) and  $R_{02}$  (blue curves) versus impact parameter for two kind of extended cloud environments (both with  $n(\text{H}_2) = 5 \times 10^3$  cm $^{-3}$  and  $T_k = 30$  K). *Upper panel:* Extended envelope alone, with  $N(\text{HCN}) = 10^{13}$  cm $^{-2}$  along its diameter, resulting in (weakly) collisionally excited HCN emission. *Lower panel:* Same envelope surrounding a dense core, with  $n(\text{H}_2) = 10^5$  cm $^{-3}$ , and scattering the bright HCN  $J=1-0$  line emission arising from the core.

larger than the core (in these models the HCN abundance is fixed to  $\chi(\text{HCN}) = 3 \cdot 10^{-9}$ ). In this case, the bright HCN  $J=1-0$  emission arising from the core is scattered by the low density envelope. For an impact parameter that crosses the envelope and not the core (i.e., an independent observation of the extended cloud) resonant scattering produces very anomalous line intensity ratios, with  $R_{12} \lesssim 0.5$  and  $R_{02} < 0.2$ . However, these ratios appear to be less frequently observed in GMCs, at least on the spatial scales of previous observations (e.g., Gottlieb et al. 1975; Loughnane et al. 2012). On the other hand, if the HCN emission intrinsically arises from low density gas far from star forming cores, the weak collisional excitation drives the intensity ratios to  $R_{12} \approx 0.6$  and  $R_{02} \gtrsim 0.2$  (upper panel of Fig. 13). The presence of high electron abundances in the envelope does not change these conclusions (dotted and dashed curves); however, as stated previously, it raises the HCN  $J=1-0$  intensities to detectable levels.

## 6. Summary and conclusions

We revisited the excitation of HCN hyperfine lines considering radiative effects and line photon exchanges induced by HFS line overlaps. Accurate models of the HCN emission require knowledge of the HFS-resolved rate coefficients for inelastic collisions of HCN with para-H<sub>2</sub> and ortho-H<sub>2</sub> (the later dominate when  $T_k > 40$  K if the H<sub>2</sub> OPR is thermalized). We computed these coefficients using the S-IO approximation up to  $J = 11$  and  $T_k = 500$  K. We also studied the role of HCN- $e^-$  collisions using HFS-resolved rates of Faure et al. (2007).

We ran a grid of static and uniform cloud models appropriate to the physical conditions in GMCs. As found by previous studies, line overlap and opacity effects alter the HFS level populations and the emitted HCN rotational spectrum when lines become optically thick, roughly at  $N(\text{HCN}) > 10^{13} \text{ cm}^{-2}$ . As a result, the relative  $J = 1-0$  HFS line intensity ratios ( $R_{12}$  and  $R_{02}$ ) deviate from the optically thin limit ratios 1:5:3 ( $R_{12} = 0.6$  and  $R_{02} = 0.2$ ). Anomalous intensity ratios imply different excitation temperatures and often different line widths for each HFS line (the basic assumption of automatic HFS line-fitting programs). In addition, the  $J = 2-1$  and  $3-2$  HFS spectra can be shown to be anomalous as well. Our models reproduce the anomalous HCN  $J = 1-0$  spectra observed in the Orion Bar and Horsehead PDRs.

As shown in previous studies focused on the HCN rotational excitation alone, electron collisions become important for H<sub>2</sub> densities below a few  $10^5 \text{ cm}^{-3}$  and electron abundances  $\chi_e > 10^{-5}$ . Electrons and line overlap effects enhance the excitation of higher  $J$  rotational levels. They enhance the emitted rotational line intensities even if the hyperfine structure is not resolved. We show that also when electron collisions dominate, the HCN  $J = 1-0$  HFS spectrum can be anomalous. In these cases, electron excitation increases the  $J = 1-0$  HFS line intensities by up to an order of magnitude if  $\chi_e \approx 10^{-4}$ , and can produce low-surface-brightness HCN emission from the low-density-gas (several  $10^3 \text{ cm}^{-3}$ ) extended environment of GMCs (tens of pc). The ubiquity of such an extended HCN emission component in GMCs, if confirmed, may affect the interpretation of the spatially unresolved extragalactic HCN emission, which may not always be dominated by dense ( $> 10^5 \text{ cm}^{-3}$ ) molecular gas – at least in normal galaxies in which  $L_{\text{HCN}}$  correlates with  $L_{\text{CO}}$ . Alternatively, the extended HCN emission in GMCs might be line photons emitted by dense molecular cores and resonantly scattered over wide spatial scales by large envelopes of lower density gas. Both scenarios produce different  $R_{12}$  and  $R_{02}$  ratios, which are more anomalous in the scattering envelope case, but currently less frequently seen in GMCs observations. Thus, the two scenarios should be tested based on observations of large-scale HCN HFS emission in galactic GMCs. All in all, we expect that a proper excitation analysis of ongoing HCN emission surveys will constrain the dominant origin and physical conditions of the HCN emitting gas in GMCs, as well as its relation with the extragalactic star formation rate correlations.

*Acknowledgements.* We thank A. Faure for sharing his HCN-HFS +  $e^-$  rate coefficients in tabulated form. We warmly thank S. Cuadrado, J. Pety, and M. Gerin for providing the HCN  $J = 1-0$  spectra of the Orion Bar and Horsehead, and for useful discussion on the HCN  $J = 1-0$  HFS emission in Orion B. We thank our referee for concise and illuminating comments. JRG and MGSM thank the Spanish MCINN for funding support under grant PID2019-106110GB-I00.

## References

Abdullah, A. & Tielens, A. G. G. M. 2020, *A&A*, 639, A110  
 Ahrens, V., Lewen, F., Takano, S., et al. 2002, *Zeitschrift Naturforschung Teil A*, 57, 669

Baudry, A., Combes, F., Perault, M., & Dickman, R. 1980, *A&A*, 85, 244  
 Ben Abdallah, D., Najjar, F., Jaidane, N., Dumouchel, F., & Lique, F. 2012, *Mon. Not. R. Astron. Soc.*, 419, 2441  
 Bergin, E. A. & Tafalla, M. 2007, *ARA&A*, 45, 339  
 Bernes, C. 1979, *A&A*, 73, 67  
 Black, J. H. & van Dishoeck, E. F. 1991, *ApJ*, 369, L9  
 Blake, G. A., Sutton, E. C., Masson, C. R., & Phillips, T. G. 1987, *ApJ*, 315, 621  
 Boisse, P. 1990, *A&A*, 228, 483  
 Bron, E., Roueff, E., Gerin, M., et al. 2021, *A&A*, 645, A28  
 Caselli, P., Walmsley, C. M., Terzieva, R., & Herbst, E. 1998, *ApJ*, 499, 234  
 Caselli, P., Walmsley, C. M., Zucconi, A., et al. 2002, *ApJ*, 565, 344  
 Cernicharo, J., Castets, A., Duvert, G., & Guilloteau, S. 1984, *A&A*, 139, L13  
 Cuadrado, S., Goicoechea, J. R., Pilleri, P., et al. 2015, *A&A*, 575, A82  
 Cuadrado, S., Salas, P., Goicoechea, J. R., et al. 2019, *A&A*, 625, L3  
 Daniel, F. & Cernicharo, J. 2008, *A&A*, 488, 1237  
 Denis-Alpizar, O., Kalugina, Y., Stoecklin, T., Vera, M. H., & Lique, F. 2013, *J. Chem. Phys.*, 224301, 139  
 Dickinson, A. S., Phillips, T. G., Goldsmith, P. F., Percival, I. C., & Richards, D. 1977, *A&A*, 54, 645  
 Elmegreen, B. G. 2007, *ApJ*, 668, 1064  
 Endres, C. P., Schlemmer, S., Schilke, P., Stutzki, J., & Müller, H. S. P. 2016, *Journal of Molecular Spectroscopy*, 327, 95  
 Evans, Neal J., I., Kim, K.-T., Wu, J., et al. 2020, *ApJ*, 894, 103  
 Falgarone, E., Phillips, T. G., & Walker, C. K. 1991, *ApJ*, 378, 186  
 Faure, A. & Lique, F. 2012, *MNRAS*, 425, 740  
 Faure, A., Lique, F., & Wiesenfeld, L. 2016, *MNRAS*, 460, 2103  
 Faure, A., Varambhia, H. N., Stoecklin, T., & Tennyson, J. 2007, *MNRAS*, 382, 840  
 Gao, Y. & Solomon, P. M. 2004a, *ApJS*, 152, 63  
 Gao, Y. & Solomon, P. M. 2004b, *ApJ*, 606, 271  
 Godard, B., Falgarone, E., Gerin, M., Hily-Blant, P., & de Luca, M. 2010, *A&A*, 520, A20  
 Goicoechea, J. R. & Cuadrado, S. 2021, *A&A*, 647, L7  
 Goicoechea, J. R., Pety, J., Gerin, M., Hily-Blant, P., & Le Bourlot, J. 2009, *A&A*, 498, 771  
 Goicoechea, J. R., Pety, J., Gerin, M., et al. 2006, *A&A*, 456, 565  
 Goicoechea, J. R., Santa-Maria, M. G., Bron, E., et al. 2019, *A&A*, 622, A91  
 Goldsmith, P. F. & Kauffmann, J. 2017, *ApJ*, 841, 25  
 Gonzalez-Alfonso, E. & Cernicharo, J. 1993, *A&A*, 279, 506  
 Gottlieb, C. A., Lada, C. J., Gottlieb, E. W., Lilley, A. E., & Litvak, M. M. 1975, *ApJ*, 202, 655  
 Guelin, M., Langer, W. D., & Wilson, R. W. 1982, *A&A*, 107, 107  
 Guilloteau, S. & Baudry, A. 1981, *A&A*, 97, 213  
 Guzmán, V., Pety, J., Goicoechea, J. R., Gerin, M., & Roueff, E. 2011, *A&A*, 534, A49  
 Guzmán, V., Roueff, E., Gauss, J., et al. 2012, *A&A*, 548, A94  
 Habart, E., Abergel, A., Boulanger, F., et al. 2011, *A&A*, 527, A122  
 Hacar, A., Hogerheijde, M. R., Harsono, D., et al. 2020, *A&A*, 644, A133  
 Hernández Vera, M., Lique, F., Dumouchel, F., Hily-Blant, P., & Faure, A. 2017, *MNRAS*, 468, 1084  
 Hollenbach, D. J., Takahashi, T., & Tielens, A. G. G. M. 1991, *ApJ*, 377, 192  
 Kauffmann, J., Goldsmith, P. F., Melnick, G., et al. 2017, *A&A*, 605, L5  
 Keto, E. & Rybicki, G. 2010, *ApJ*, 716, 1315  
 Kwan, J. & Scoville, N. 1975, *ApJ*, 195, L85  
 Lada, C. J. & Lada, E. A. 2003, *ARA&A*, 41, 57  
 Lada, C. J., Lombardi, M., & Alves, J. F. 2010, *ApJ*, 724, 687  
 Langer, W. D., Wilson, R. W., Henry, P. S., & Guelin, M. 1978, *ApJ*, 225, L139  
 Lanza, M. & Lique, F. 2014, *J. Chem. Phys.*, 141, 164321  
 Lapinov, A. V. 1989, *Soviet Ast.*, 33, 132  
 Liszt, H. & Lucas, R. 2001, *A&A*, 370, 576  
 Liszt, H. S. 2012, *A&A*, 538, A27  
 Loughnane, R. M., Redman, M. P., Thompson, M. A., et al. 2012, *MNRAS*, 420, 1367  
 Magalhães, V. S., Hily-Blant, P., Faure, A., Hernandez-Vera, M., & Lique, F. 2018, *A&A*, 615, A52  
 Maloney, P. R., Hollenbach, D. J., & Tielens, A. G. G. M. 1996, *ApJ*, 466, 561  
 Maret, S. & Bergin, E. A. 2007, *ApJ*, 664, 956  
 Meijerink, R. & Spaans, M. 2005, *A&A*, 436, 397  
 Melnick, G. J., Tolls, V., Snell, R. L., et al. 2020, *ApJ*, 892, 22  
 Monteiro, T. S. & Stutzki, J. 1986, *MNRAS*, 221, 33P  
 Mullins, A. M., Loughnane, R. M., Redman, M. P., et al. 2016, *MNRAS*, 459, 2882  
 Neufeld, D. A. & Green, S. 1994, *ApJ*, 432, 158  
 Neufeld, D. A., Melnick, G. J., Sonnentrucker, P., et al. 2006, *ApJ*, 649, 816  
 Nishimura, Y., Watanabe, Y., Harada, N., et al. 2017, *ApJ*, 848, 17  
 Pabst, C. H. M., Goicoechea, J. R., Teyssier, D., et al. 2017, *A&A*, 606, A29  
 Pabst, C. H. M., Hacar, A., Goicoechea, J. R., et al. 2021, *A&A*, 651, A111  
 Pety, J., Gratier, P., Guzmán, V., et al. 2012, *A&A*, 548, A68  
 Pety, J., Guzmán, V. V., Orkisz, J. H., et al. 2017, *A&A*, 599, A98

- Phillips, T. G., Huggins, P. J., Wannier, P. G., & Scoville, N. Z. 1979, *ApJ*, 231, 720
- Pineda, J. L., Langer, W. D., Velusamy, T., & Goldsmith, P. F. 2013, *A&A*, 554, A103
- Punanova, A., Caselli, P., Pineda, J. E., et al. 2018, *A&A*, 617, A27
- Roueff, E. & Lique, F. 2013, *Chemical Reviews*, 113, 8906
- Salas, P., Rugel, M. R., Emig, K. L., et al. 2021, *A&A*, 653, A102
- Santa-Maria, M. G., Goicoechea, J. R., Etxaluze, M., Cernicharo, J., & Cuadrado, S. 2021, *A&A*, 649, A32
- Schilke, P., Walmsley, C. M., Pineau Des Forets, G., et al. 1992, *A&A*, 256, 595
- Shimajiri, Y., André, P., Braine, J., et al. 2017, *A&A*, 604, A74
- Shirley, Y. L. 2015, *PASP*, 127, 299
- Snow, T. P. & McCall, B. J. 2006, *ARA&A*, 44, 367
- Sofia, U. J., Lauroesch, J. T., Meyer, D. M., & Cartledge, S. I. B. 2004, *ApJ*, 605, 272
- Sohn, J., Lee, C. W., Park, Y.-S., et al. 2007, *ApJ*, 664, 928
- Stutzki, J. & Guesten, R. 1990, *ApJ*, 356, 513
- Thorwirth, S., Müller, H. S. P., Lewen, F., et al. 2003, *ApJ*, 585, L163
- Turner, B. E., Pirogov, L., & Minh, Y. C. 1997, *ApJ*, 483, 235
- van Dishoeck, E. F. & Black, J. H. 1989, *ApJ*, 340, 273
- Vera, M. H., Kalugina, Y., Denis-Apizar, O., Stoecklin, T., & Lique, F. 2014, *J. Chem. Phys.*, 140, 224302
- Walker, K. M., Yang, B. H., Stancil, P. C., Balakrishnan, N., & Forrey, R. C. 2014, *ApJ*, 790, 96
- Walmsley, C. M., Churchwell, E., Nash, A., & Fitzpatrick, E. 1982, *ApJ*, 258, L75
- Zhang, J. S., Liu, W., Yan, Y. T., et al. 2020, *ApJS*, 249, 6
- Zinchenko, I., Forsstrom, V., & Mattila, K. 1993, *A&A*, 275, L9
- Zinchenko, I. I. & Pirogov, L. E. 1987, *Soviet Ast.*, 31, 254

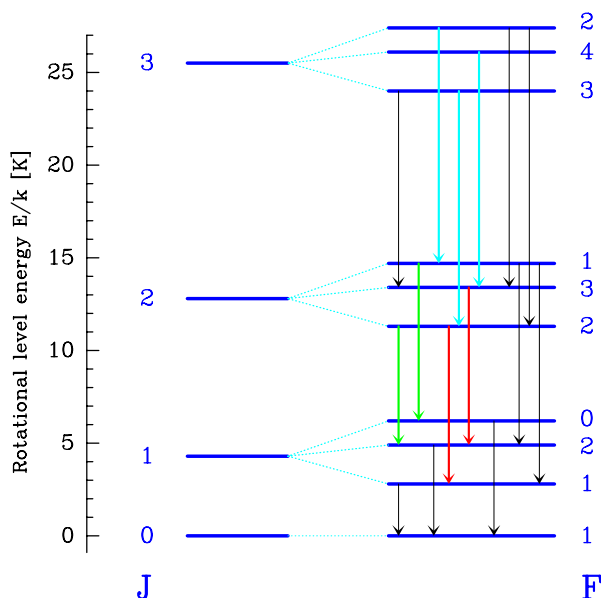


**Fig. A.1.** HCN rotational energy diagram and HFS splittings (exaggerated for clarity). Arrows show dipole-allowed radiative transitions. Red, green, and cyan arrows show lines that overlap, in interstellar conditions, and produce most of the anomalous HFS emission discussed in the text.

## Appendix A: HCN HFS energy diagram

Figure A.1 shows the low-lying HCN rotational levels and HFS structure taken from CDMS (Endres et al. 2016) using spectroscopic data from Ahrens et al. (2002); Thorwirth et al. (2003), and references therein.

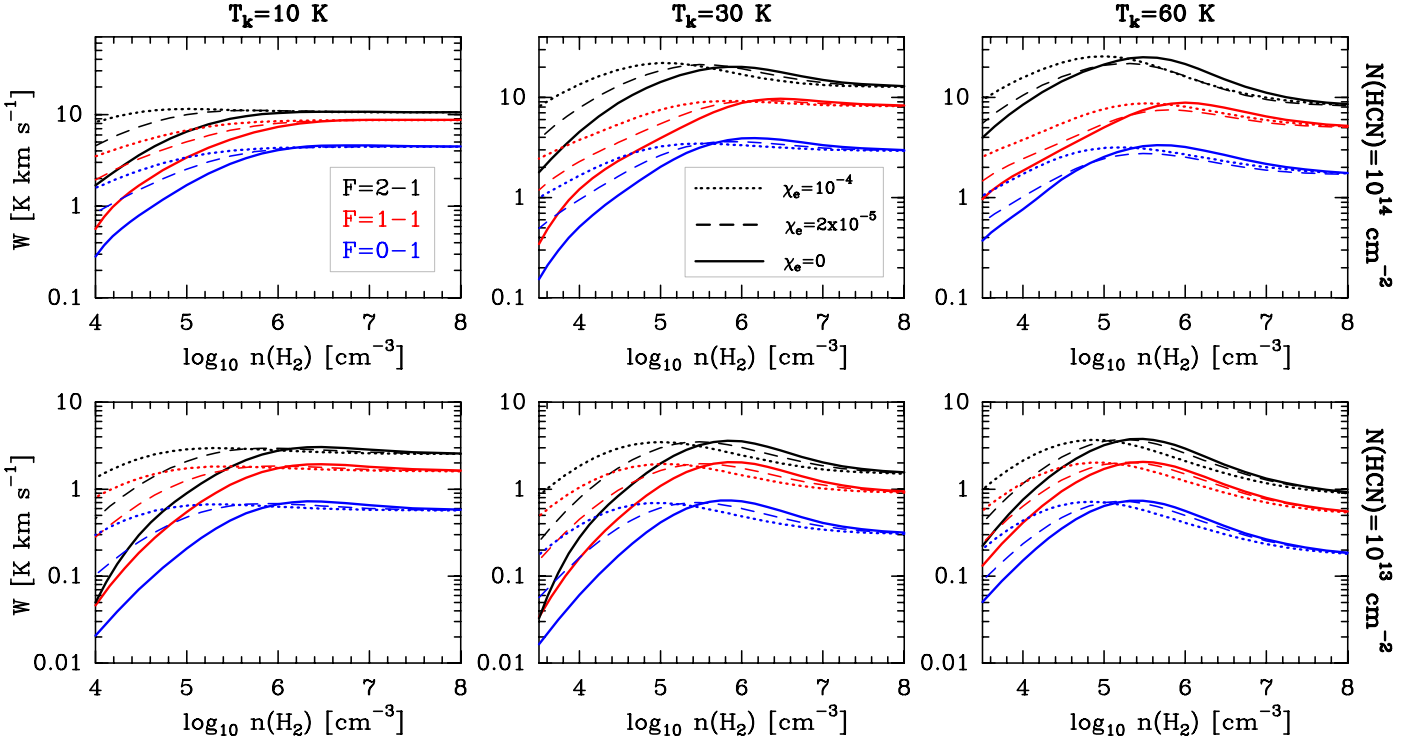
## Appendix B: Absolute line intensities

Figure B.1 shows absolute intensities of the HCN  $J = 1-0$ ,  $2-1$ , and  $3-2$  lines (integrating over all HFS components) from our grid of static cloud models including line overlap effects and three different electron abundances:  $\chi_e = 0$  (continuous curves),  $\chi_e = 2 \cdot 10^{-5}$  (dashed), and  $\chi_e = 10^{-4}$  (dotted).

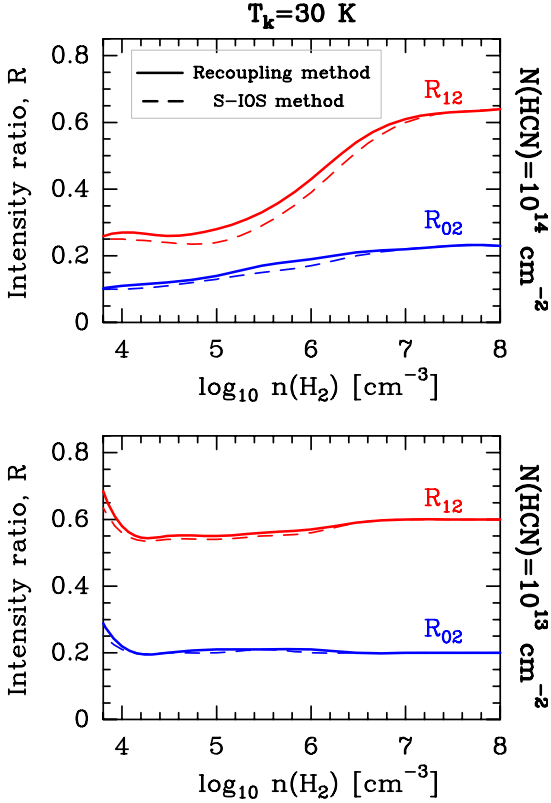
## Appendix C: Recoupling vs. S-IOS HCN–H<sub>2</sub> HFS rate coefficients

Figure C.1 shows the effects of using the H<sub>2</sub>–HCN HFS collisional rate coefficients computed in the S-IOS approximation (dashed lines) and using rates in the nearly exact recoupling method (continuous curves) of Magalhães et al. (2018). These are cloud models at  $T_k = 30$  K ( $H_2$  OPR  $\approx 0.03$ ). Thus, they only consider collisions with para-H<sub>2</sub>. For optically thin or slightly thick lines (models with  $N(\text{HCN}) = 10^{13} \text{ cm}^{-2}$ ) line overlap effects are very minor, the resulting  $R_{12}$  and  $R_{02}$  ratios using different collisional rate datasets are nearly identical (bottom panel in Fig. C.1). For higher  $N(\text{HCN})$  and  $\tau_{\text{hfs}}$ , line overlap effects become important. Despite the slightly different rate coefficients, especially the quasi-elastic rates ( $\Delta J = 0$ ), the  $R_{12}$  and  $R_{02}$  ratios are only (up to)  $\sim 15\%$  lower than in models that use the more approximated S-IOS rates. The absolute line intensities only differ by a few percent. Therefore, we conclude that the adoption of rates calculated in the S-IOS approximation at high  $T_k$  should be accurate enough in most astrophysical applications. Hence, it benefits from the use of HFS-resolved rates for collisions with both ortho-H<sub>2</sub> and para-H<sub>2</sub> and at higher gas temperatures.





**Fig. B.1.** HCN  $J=1-0$  HFS integrated line intensities;  $I(F_u-F_l)$  in  $\text{K km s}^{-1}$ . Model results show the role of electron excitation for different ionization fractions:  $\chi_e = 0$  (continuous curves),  $\chi_e = 2 \cdot 10^{-5}$  (dashed), and  $\chi_e = 10^{-4}$  (dotted). All models include line overlap.



**Fig. C.1.**  $J=1-0$  HFS integrated line intensity ratios  $R_{12} = I(F=1-1)/I(F=2-1)$  and  $R_{02} = I(F=0-1)/I(F=2-1)$  using different methodologies to compute the collisional rate coefficients at  $T_k = 30 \text{ K}$ : recoupling (continuous curves) and S-IOS (dashed lines).